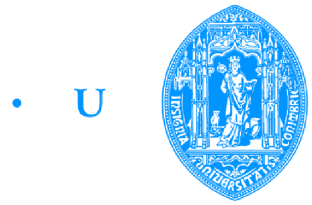

UNIVERSIDADE DE COIMBRA

Hydrogen impurity in paratellurite α-TeO_2 using Muon-spin rotation

Dissertação submetida para a obtenção do Grau de Mestre em Física com especialização em Física da Matéria Condensada

Ricardo Borda Lopes Vieira

Orientador: Professor Doutor Rui César do Espírito Santo Vilão

Coimbra, 2011

Para a Tânia
O Gabriel
E os meus Pais

Abstract

We have investigated the behavior of isolated hydrogen in paratellurite (α-TeO_2) by means of muon-spin rotation spectroscopy (μSR) measurements. The observable metastable states accessible by means of the muon implantation allowed us to probe both the donor and the acceptor configurations of hydrogen, as well as to follow their dynamics. A shallow donor state with an ionization energy of 6 meV, as well as a deep acceptor state are proposed. From the experimental μSR results, the donor (+/0) conversion level was located near the conduction band edge, consistent with DFT results. Atom-like interstitial muonium was also observed; it has a hyperfine interaction of about 3.5 GHz, possibly slightly anisotropic.

Possible site exchange (deep to shallow conversion) and charge exchange high temperature dynamics are discussed, and a dynamical model for the formation of Mu^- is discussed and simulated.

Preliminary work on yttrium oxide (Y_2O_3) is also presented, as well as, possible hydrogen configurations.

Resumo

Investigámos o comportamento de hidrogénio isolados em paratellurite (α-TeO_2), por meio de medições espectroscopia de muão positivo (μSR). Os estados metaestáveis observáveis acessíveis por meio da implantação do muão permitiram-nos sondar as configurações dadora e aceitadora do hidrogénio, bem como acompanhar a sua dinâmica. Um estado dador "superficial" com uma energia de ionização de 6 meV, bem como um estado aceitador profundo são propostos. A partir dos resultados experimentais de μSR, o nível de conversão do dador (+/0) estava localizado perto da banda de condução, consistente com os calculos DFT. Muonium intersticial com comportamento quasi-Atómico também foi observado com uma interação hiperfina de cerca de 3,5 GHz, possivelmente com uma ligeira anisotropia.

Possíveis dinâmicas do tipo "site exchange" (conversão de muonium aceitador a dador) e do tipo "charge exchange" (modelo da dinamica de Mu^-), são discutidas para o caso das temperaturas altas, sendo uma simulação feita para o caso do modelo da dinâmica de Mu^-.

Trabalho preliminar sobre óxido de ítrio (Y_2O_3) também é apresentado, bem como possíveis configurações de hidrogénio nesse semicondutor.

Acknowledgements

It is a pleasure to thank the many people who made this thesis possible.

Foremost, I would like to express my sincere gratitude to my advisor Prof. Rui César do Espírito Santo Vilão for the continuous support of my M. Sc. study and research, for his patience, motivation, enthusiasm, and immense knowledge. His guidance helped me in all the time of research and writing of this thesis. I could not have imagined having a better advisor and mentor for my M. Sc. study.

Besides my advisor, I would like to thank the rest of the CEMDRX group for enlightening me the first glance of research and for giving me the opportunity to go to PSI and ISIS laboratories, with special emphasis to Prof. Dr. João Campos Gil, Prof. Dr. Helena Vieira Alberto, Prof. Dr José António Paixão and Prof. Dr. Apostolos Marinopoulos.

I appreciate the the devotion given by my school teachers José Manuel and Teresa Duarte.

I thank my friends: Estelina, Gafeira, Inês, Joana, Mamede, Miguel, Nuno, Pedro Melo, Pedro, R. Martins, Rosado, Susana,Tiago, everyone from GBU, Alves, Jill, Josué, Manuel, Mipi, P.B., Pio, Roque, Ruben G., Salu, ... for all the leisure and work time spent together.

Last but not the least, I would like to thank my family: my wife Tânia Vieira, my son Gabriel, my brother, and my parents Anibal, Bela, Lola and Paulo, for their patience and love.

Contents

List of Figures

List of Tables

Chapter 1

Hydrogen in semiconductors

"Hydrogen is the simplest element of the Periodic Table."
(unknown, often quoted, and incorrect source) [7]

1.1 Introduction

The simple structure of the hydrogen atom from the atomic physicist's perspective may inspire the idea that hydrogen is the simplest element in the Periodic Table. However, that simplicity is not present at all in the behavior of the hydrogen impurity in semiconductors. In fact, the behavior of the hydrogen impurity in semiconductors is found to be rather complex.

The most important effects due to hydrogen in a semiconductor are:

- Formation of a variety of (isolated) atomic configurations, with the corresponding introduction of levels in the band gap [8, 9];
- Formation of complexes with other impurities and defects [10];
- Formation of H_2 molecules [11];
- Inducing hydrogen-related extended defects [12].

The reason for the immense interest in the study of the hydrogen impurity in semiconductors is arisen from the fact that it can be found in numerous semiconductors as an unwanted impurity. Hydrogen can be incorporated

in semiconductors in the growth or treatment processes: it can either be present in the growth, e.g. $Zn(CH_3)_2 + H_2O \rightarrow ZnO + 2CH_4$; or it can be incorporated by annealing processes and chemomechanical polishing.

1.2 Compensation / Passivation

Hydrogen may contribute to the electrical properties of semiconductors by two essentially distinct processes: passivation and compensation/dominant dopant (isolated hydrogen).

The main difference between them is that whereas passivation implies the formation of a complex (hydrogen-defect/impurity), compensation implies that hydrogen remains isolated.

They can be distinguished experimentally by Hall effect measurements with varying hydrogen concentration in the semiconductor. If the predominant effect is passivation, the Hall voltage measured should increase with the increasing hydrogen concentration, because the mobility of the charge carriers should increase. If the predominant effect is compensation, the Hall voltage measured should decrease with the increasing hydrogen concentration, because the mobility of the charge carriers should decrease.

Passivation effects are widely studied and complexes are observed with defects and with impurities. The most common example is the passivation of dangling bonds [13]. This passivation phenomenon removes unwanted electron energy levels from the bandgap, thus increasing the mobility of the carriers and allowing technology such as solar cells or thin-film transistors [14]. The passivation of the boron acceptor in Si [10] constitutes an example of passivation of impurities, where the formation of a B-H complex reduces the acceptor effects of boron.

1.3 Isolated Hydrogen in Semiconductors

In systems such as silicon and zinc oxide, where intensive research on isolated hydrogen has been done, two distinct configuration states have been

identified: H^-at an interstitial position and, H^+ at a bonded position (bond-center in Si, antibonding in ZnO), together with the respective neutrals [15, 16]. The use of positive muons to study these configurations has been very successful, in contrast with the difficulties found by techniques sensitive to protons themselves, due to the reactivity of hydrogen in semiconductors. The positions of the (bonded) donor (0/+) and (interstitial) acceptor (–/0) energy levels in the bandgap, have been obtained for isolated hydrogen in various semiconductors, using different techniques. Table 1.1 shows the level positions in Si as determined by several experimental techniques or determined from ab initio calculations. A slight difference is expected, for the μSR results, due to differences in the proton and muon zero point motion.

Table 1.1: Position of the (isolated) hydrogen donor (0/+) and acceptor (–/0) energy conversion level in the Si bandgap, as determined by several experimental methods and by first-principles calculations [6].

Method	ϵ(0/+)	ϵ(–/0)
Muon implantation (μSR)	0.21 eV [17]	$<$ 0.56 eV [15]
Proton implantation (DTLS)	0.16 eV [18]	0.65 eV [19]
Dissociation of P-H complexes [20]	0.16 eV	0.67 eV
First-principles calculations [21]	0.2 eV	0.6 eV

In this context it is practical to discuss about Anderson's U model [22]. U is a quantity defined by U = ϵ(0/–) – ϵ(+/0), were ϵ(a/b) is the energy of the a/b level. In this schema we can predict two possible outcomes: positive-U and negative-U. Positive-U corresponds to the expected relative position of the two levels, taking in to account that the energy to ionize a single occupied state is larger then the energy to ionize a doubly occupied state. By opposition negative-U implies that the energy to ionize a doubly occupied state is larger then the energy to ionize a single occupied state. This can

happen only if the energy associated to the site change compensates the coulombic repulsion of the two electrons.

Using this model, simply by knowing the nature of U, we can determine if H^0 is thermodynamically stable. In Fig.1.1 [1] we see that in negative-U (a) H^0 is unstable and in positive-U (b) H^0 is sable.

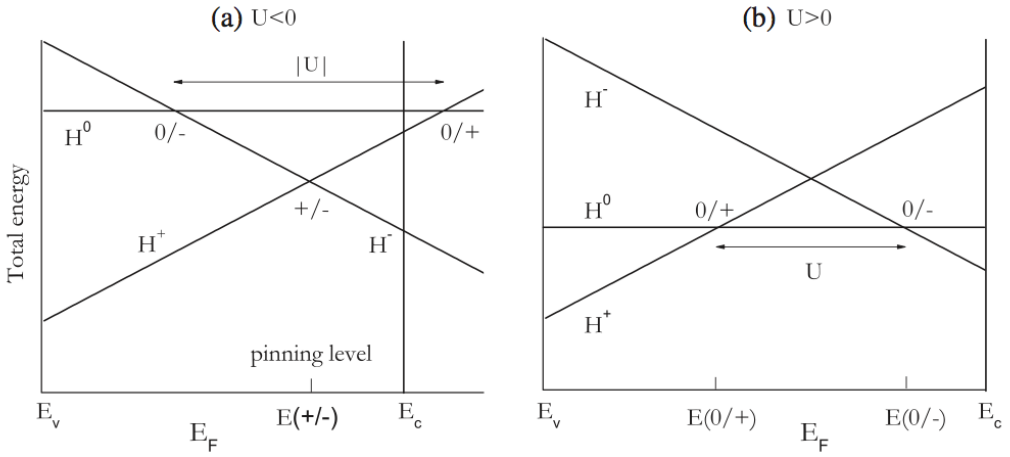

Figure 1.1: Formation energies of a hydrogen defect centre as a function of Fermi level EF. The gradient with respect to EF is equal to the charge; Ev is the top of the valence band and Ec the bottom of the conduction band. (a) is drawn for negative U, and with the 0/+ donor level resonant with the conduction band. This leads to auto-ionization of the neutral state (shallow-donor behaviour) but the material will only be conductive under equilibrium conditions if the +/– pinning level is also band-resonant; here it is shown deep in the gap. (b) is drawn for positive U , leading to the opposite ordering of 0/+ and 0/– transition points, both shown deep in the gap [1].

A note on density-functional theory (DFT)

The present experimental study was complemented by *ab-initio* calculations based on density-function theory, done by Dr. Apostolos Marinopoulos [2], which will be used in order to strengthen the interpretation. For the sake of clarity only, we add a brief note on the fundamentals of DFT theory.

DFT is a many-body electronic structure calculation where the nuclei of the treated molecules or clusters are seen as fixed (Born-Oppenheimer approximation) [5], generating a static external potential V in which the electrons are moving. Then, a wavefunction satisfying the many-electron time-independent Schrödinger equation describes the stationary electronic state, were the hamiltonian can be written as:

$$H = \sum_{i=1}^{N} -\frac{1}{2}\nabla_i^2 + \sum_{i=1}^{N} v(\vec{r_i}) + \sum_{i<j}^{N} -\frac{1}{r_{ij}} = T + V_{pe} + V_{ee} \tag{1.1}$$

where T is the kinetic energy, V_{pe} is the potential energy from the external field due to positively charged nuclei, and V_{ee} is the electron-electron interaction energy.

In this theory the key variable is the particle density $n(\vec{r})$ which for a normalized wavefunction is given by:

$$n(\vec{r}) = N \int |\Psi(\vec{r_1}, ..., \vec{r_N})|^2 d\vec{r_2}, ..., d\vec{r_N} \tag{1.2}$$

From the Hohenberg-Kohn theorems we know that the energy is a density functional and can be solved by applying the Lagrangian method of undetermined multipliers.

A simple way to do that is to consider an energy functional, E_s[n], that doesn't explicitly have an electron-electron interaction energy term:

$$E_s[n] = \langle \Psi_s[n] | T + V_s | \Psi_s[n] \rangle \tag{1.3}$$

where V_s is an external effective potential in which the particles are moving.

The second Hohenberg-Kohn theorem ensures that when the energy is written as a functional of some particular (positive) density, then its value is always larger than the ground state energy. This provides the necessary variational principle from which the Kohn-Sham equations are derived:

$$\frac{\delta E}{\delta n} = 0 \tag{1.4}$$

From this variational principle the effective Kohn-Sham potential can be derived:

$$V_s(\vec{r}) = V(\vec{r}) + \int \frac{e^2 n_s(\vec{r'})}{|\vec{r} - \vec{r'}|} d^3r' + V_{xc}[n_s(\vec{r})]. \tag{1.5}$$

The second term denotes the Hartree term describing the electron-electron Coulomb repulsion, while the last term is called the exchange-correlation potential, which includes all the many-particle interactions. The problem of solving the Kohn-Sham equation is then done in a self-consistent (i.e., iterative) way. Usually one starts with an initial guess for $n(\vec{r})$, then calculates the corresponding V_s and solves the Kohn-Sham equations. Then one calculates a new density and starts again. This procedure is then repeated until convergence is reached.

1.4 Isolated hydrogen in Paratellurite (α-TeO_2)

Since the discovery that the hydrogen impurity may play an active role as a source of n-type conductivity in ZnO, the investigation of the role of hydrogen in oxides has assumed increasing and vital importance: this prediction was made theoretically from calculations based on density-functional theory (DFT) [24] and first confirmed experimentally by muon-spin rotation (μSR) spectroscopy [16]. The identification of shallow-donor hydrogen levels was subsequently generalized to other related systems [25–28].

The interest in studying α-TeO_2 (paratellurite) is its relevance among the semiconducting oxide non-linear optical materials [29] as well as it being a promising active material for optical devices, [30–32] gas sensors [33, 34] or as for the search of neutrinoless beta decay [35]. Research by ab-initio DFT and molecular-orbital approaches [29, 36–38] have also been made in order to study its structure, vibrational and optical properties. High dielectric constants have been reported [38, 39], which may include α-TeO_2 in the list of possible candidates for the replacement of SiO_2 as gate oxide material in highly miniaturized transistors [40]. A limited number of studies have bem made on the conductivity of α-TeO_2, mostly concentrated on the behavior

at or above room temperature. Impurities seem to play a determinant role at room temperature, where p-type conductivity seems to be dominant, [41] although evidence for n-type conductivity has been found as well (Ref. [6] from Ref. [41]). Hydrogen is present during the growth and is (unwillingly) incorporated into the material and evidence of its interaction with other dopant ions and oxygen vacancies (V) has been suggested: both the Cr^{3+}–VO–2H centre [42] and the V^{4+}–2H centre [43] have been characterized.

In Figure 1.2 we show the corresponding formation energies as a function of the Fermi-level position in the band gap for all different minimum-energy configurations that hydrogen can exist for each of its charge states [2]. Theses calculations have been done by Dr. Apostolos Marinopoulos, in a theoretical work parallel to this experimental research work, which contributed to a joint publication [2]. We see that the donor level $\epsilon(+/0)$ lies higher in the gap compared to the acceptor level $\epsilon(0/-)$. This inequality suggests that the DFT calculations predict hydrogen to be a negative-U defect in α-TeO_2. Nonetheless, both H^0 and H^- can exist in more than one configuration in the lattice (see Fig. 1.4) and when comparing with μSR these higher-energy metastable configurations are still relevant, since non-equilibrium processes occurring at a very short time scale can be accessed the experimental method. That is the reason the formation energies associated with all existing multiple configurations are also shown in 1.2. New displaced transition levels become possible, due to these metastable configurations, that connect the higher-energy charge states of hydrogen for each different geometrical configuration. These are indicated by arrows in Fig. 1.2 where it can be seen that the acceptor level $\epsilon(0/-)$ is progressively displaced closer to the valence-band edge.

A strong tendency, that all charged states displayed was, interstitial hydrogen binding to the bridging oxygen atoms (rendering them three-fold coordinated) with a formation of a strong covalent O-H bond with a length of 0.98 Å. The corresponding equilibrium configuration for hydrogen in the positive charge state, H^+, is shown in Fig. 1.4a.

Hydrogen was also found to adopt this bond configuration in its neutral state, H^0. As seen before, no deep state in the gap appears: the additional

electron occupies an energy level that is resonant with the conduction band, rendering hydrogen effectively ionized with its electron in a delocalized state. We can in Fig.1.2 see that the calculated donor level $\epsilon(+/0)$ is nearly degenerate with the conduction-band minimum, CBM. By exploring further the configurational space of neutral hydrogen, H^0, in the lattice It was found that H^0 possesses another stable configuration of higher energy (by 1.3 eV), by exploring the configurational space of neutral hydrogen, H^0, in the lattice, where the hydrogen atom resides at an interstitial site deeper in the interior of the ring (see Fig. 1.4b). Hydrogen is located close to its nearest tellurium ion at a distance of 1.75 Å, with the next nearest neighbors being two oxygen ions across the ring at distances in the 1.90 – 2.20 Å range. Two different configurations are possible in the egatively charged H^- case, as we shall now discuss. The electron charge density of this level is plotted in Fig.1.3a. It can be seen that the state is relatively localized at the hydrogen itself in an approximately spherically-symmetric charge distribution, but carries also considerable weight at ions of its immediate vicinity, most notably its tellurium nearest neighbor.

The previously described interstitial configuration was also found to be stable for the negatively-charged hydrogen, H^-, in contrast to H^0 and H^+. However, the bond configuration discussed above has a higher energy (almost by 1 eV) and it was found to be unstable under small perturbations, especially with respect to displacements of the oxygen ion (participating in the OH^- bond) along the c axis (see Fig. 1.4c). This instability leads to a new stable H^- configuration of lower energy with respect to the interstitial state (Fig. 1.2). This H^- state, depicted in Fig. 1.4c, is a rather extended defect complex. It comprises an OH^- bond, that this time is no longer perpendicular to the c axis, and a pair of under- and over- coordinated tellurium ions in its immediate vicinity, Te[3] and Te[5]. The oxygen ion participating in the OH^- bond has displaced considerably from its initial position in the lattice leaving behind a three- fold coordinated tellurium (Te[3]), and creating an over- coordinated one (Te[5]). This negatively-charged state possesses a defect level deep in the band gap, occupied by two electrons. While the, the positively-charged state was unstable, the defect-complex configuration

persists (with some changes in the local structure) as a neutral state. This neutral state, therefore, is the third stable H^0 configuration in α-TeO2 with a singly-occupied deep level in the gap and an energy slightly higher to the energy of the neutral H0 bond state discussed earlier (Fig. 1.2). The charge-density distribution for this level, shown in Fig.1.3b, is localized near the O–H bond and displays a strong asymmetry with a large weight on the undercoordinated tellurium ion, Te[3].

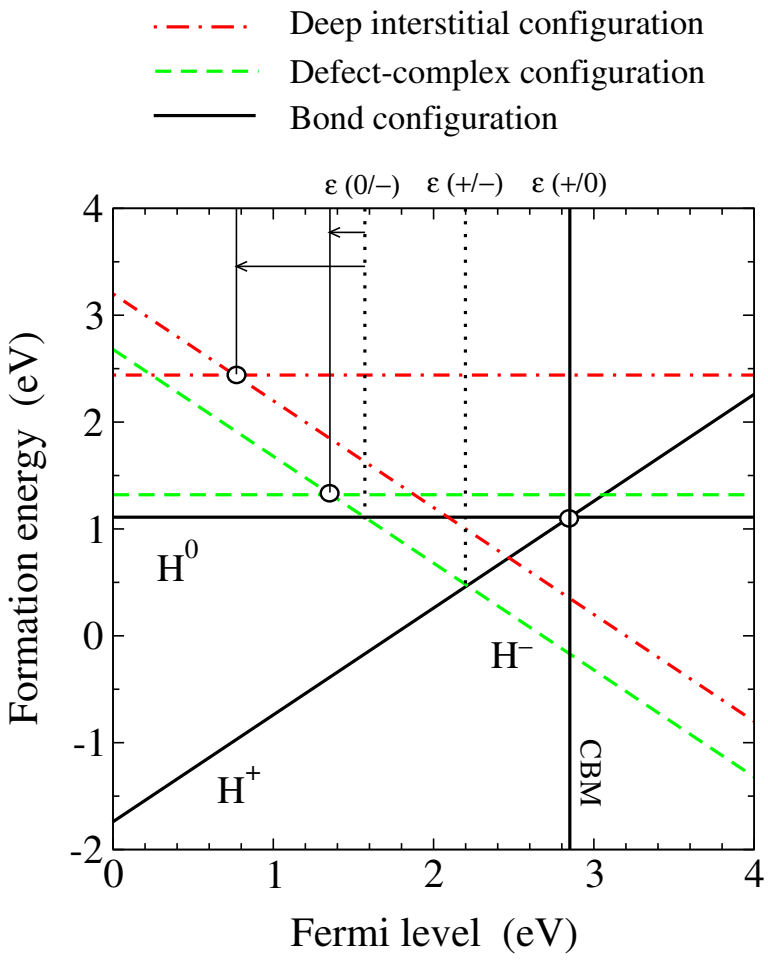

Figure 1.2: Formation energies of the different charge states of hydrogen versus Fermi-level position in the band gap. The energies for all multiple minimum-energy configurations discussed in the text are included as well, with corresponding labels shown above the plot. The thermodynamic defect transition levels, $\epsilon(q, q')$, are denoted by the vertical dotted lines. The positions of the acceptor levels $\epsilon(0/-)$ among the H^0 and H^- states stable at different geometric configurations are also explicitly shown by the arrows. The solid vertical line, marked as CBM, denotes the theoretical DFT conduction-band minimum. The reference energy for the Fermi level is set at the valence band maximum [2].

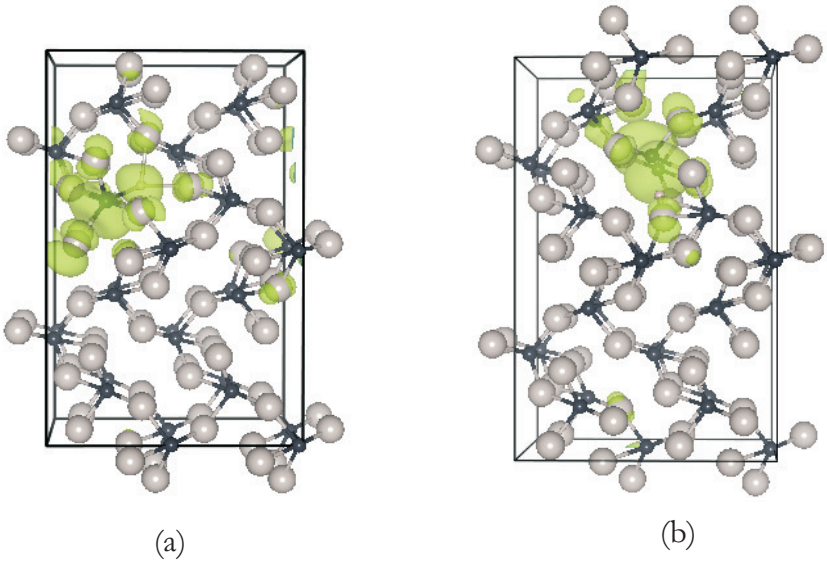

Figure 1.3: Isosurfaces (in color) of the electron charge densities for the defect level in the gap in the higher-energy deep interstitial H^0 configuration (a) and in the intermediate-energy defect-complex H^0 configuration (b). The full supercell is shown for both cases, in a projection parallel to the **b**-lattice vector [2].

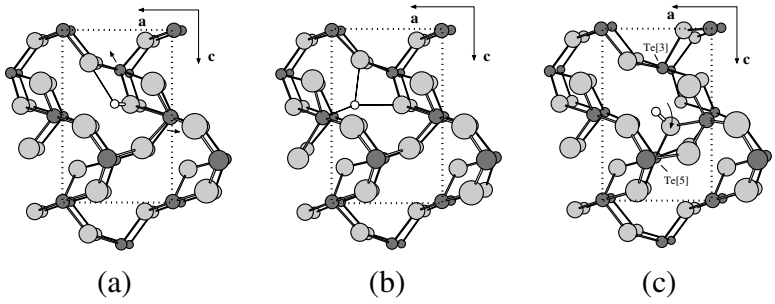

Figure 1.4: Minimum-energy configurations of isolated hydrogen (small white circle) in α-TeO_2, shown in a projection parallel to the **b**-lattice vector. Oxygen and tellurium ions are depicted as the larger and lighter (smaller and darker) circles, respectively. Dotted lines denote the bulk-crystal repeating unit. (a) Bond configuration; (b) High-energy deep interstitial configuration; (c) Defect-complex-acceptor-like configuration [2].

Chapter 2

μSR Techniques

2.1 Introduction

μSR is the designation given to the set of experimental techniques which use positive or negative muons as probes in condensed matter or gases.

In this work only positive muons and positive μSR techniques were used, which we will shortly refer to as muons and μSR, respectively.

In μSR studies, positive muons are viewed as light isotopes of hydrogen, and used as probes to study hydrogen effects (as described in the previous chapter).

This is possible because the proton and muon properties are similar, as are also the muonium and hydrogen properties. We can confirm that in tables 2.1 [6] and 2.2 [6] below.

We see that the majority of the chemical properties are similar except for the mass, which do not affect the electronic properties and the chemistry that we are studying. It is expected that the hyperfine frequencies measured are higher in muon studies, then in proton studies, because of the higher hyperfine parameter.

Table 2.1: [6] Muon and proton properties compared. The muon's mass is approximately 1/9 of the the proton's mass m_{p} and its gyromagnetic ratio $\gamma_\mu = g_\mu \, \mu_\mu / h$ is larger than the proton's by approximately a factor of 3 [6].

	muon	**proton**
charge/e	+1	+1
spin/$\hbar$	1/2	1/2
mass/m_{p}	0.1126	1
Gyromagnetic ratio (MHz T^{-1})	135.54	42.58
Lifetime/μs)	2.19703	stable

Table 2.2: [6] Muonium (Mu) and hydrogen (H) properties compared. The factor of 3 between the hyperfine parameter of ground state muonium and ground state protium basically arises from the corresponding relation between the nuclei magnetic moments, the electron density at the nucleus being basically the same: when scaling the hyperfine parameter of Mu by the nuclei magnetic moment relation we obtain 1402 MHz [6].

	Mu	**H**
Reduced mass (m_{e})	0.995187	0.999456
Binding energy in the ground state (eV)	13.54	13.60
Hyperfine parameter (MHz)	4463	1420.4
Gyromagnetic ratio/ (MHz T^{-1})	135.54	42.58
Atomic radius in the ground state (Å)	0.531736	0.529465

2.2 Muonium

Muonium spectroscopy is based upon the knowledge which allows to measure the strength of the interaction between the spin of the muon and that of the electrons. We dedicate this part of this work for a brief summery of the essential physics of the hyperfine interactions in muonium.

Intense research on the vacuum hyperfine structure of this exotic atom has been done in the past decades [44–48], serving as precise tests in quantum electrodynamics. However, when muonium is formed inside solids, its hyperfine structure is much affected by the local electronic structure, which makes it a rather sensitive probe.

In most cases two distinct configurations can be formed: isotropic muonium (also labelled normal), in the case were the electron wavefunction is still isotropic (i.e. spherically symmetric) and a bonded configuration (also labelled "anisotropic" or "anomalous" muonium) characterized by an axially symmetric wave function.

2.2.1 Isotropic muonium

For $1s$ isotropic muonium, the relevant hyperfine hamiltonian simply corresponds to the well-known Fermi contact interaction [49] between the muon spin $\mathbf{S}_\mu$ and the electron spin $\mathbf{S}_e$ [6, 50]:

$$H = hA\mathbf{S}_\mu \cdot \mathbf{S}_e \tag{2.1}$$

where the hyperfine interaction A is simply proportional to the electron density at the muon $|\Psi_{1s}(r=0)|^2 = 1/\pi a_0^3$:

$$A = \frac{\mu_0}{4\pi}\frac{8}{3}\frac{g_\mu \mu_\mu g_e \mu_B}{a_0^3} = \frac{\mu_0}{4\pi}\frac{8\pi}{3} g_\mu \mu_\mu g_e \mu_B \left|\Psi_{1s}(r=0)\right|^2 \tag{2.2}$$

where $g_\mu = 2$, $g_e = 2$, $\mu_\mu = e\hbar/2m_\mu$ and $\mu_B = e\hbar/2m_e$ are the muon gyromagnetic factor, electron gyromagnetic factor, muon magneton and Bohr magneton, respectively. μ_0 is the magnetic permeability of the free space and a_0 is the Bohr radius.

The muon and electron Zeeman terms should be added to the hamiltonian 2.1 because μSR techniques are undertaken in the presence of an external applied magnetic field $\mathbf{B}$:

$$H = hA\mathbf{S}_\mu \cdot \mathbf{S}_e - \mathcal{M}_\mu \cdot \mathbf{B} - \mathcal{M}_e \cdot \mathbf{B} \tag{2.3}$$

where the muon and electron magnetic moment operators $\mathcal{M}_\mu$ and $\mathcal{M}_e$ can be explicited in terms of the corresponding spin operators as:

$$\mathcal{M}_\mu = \frac{g_\mu \, \mu_\mu}{\hbar}\mathbf{S}_\mu \tag{2.4}$$

$$\mathcal{M}_e = -\frac{g_e \, \mu_B}{\hbar}\mathbf{S}_e \tag{2.5}$$

where the muon magneton μ_μ and the Bohr magneton μ_B are given, as usual, by:

$$\mu_\mu = \frac{e\hbar}{2m_\mu} \tag{2.6}$$

$$\mu_B = \frac{e\hbar}{2m_e} \tag{2.7}$$

We assume that $\mathbf{B} = B\hat{\mathbf{k}}$, without loss of generality, leading us to:

$$H = hA\mathbf{S}_\mu\cdot\mathbf{S}_e - \frac{g_\mu \, \mu_\mu \, B}{\hbar}\hat{\mathbf{S}}_{\mu,z} + \frac{g_e \, \mu_B \, B}{\hbar}\hat{\mathbf{S}}_{e,z} = hA\mathbf{S}_\mu\cdot\mathbf{S}_e - \omega_\mu\hat{\mathbf{S}}_{\mu,z} + \omega_e\hat{\mathbf{S}}_{e,z} \tag{2.8}$$

where

$$\omega_e = 2\pi\gamma_e \, B \tag{2.9}$$

$$\omega_\mu = 2\pi\gamma_\mu \, B \tag{2.10}$$

and the muon and electron gyromagnetic ratios are, respectively,

$$\gamma_\mu = g_\mu \mu_\mu / h = 135.53\,\mathrm{MHz/T} \tag{2.11}$$

$$\gamma_e = g_e \mu_B / h = 28024.21\,\mathrm{MHz/T} \tag{2.12}$$

Hamiltonian 2.8 can be equivalently expressed as:

$$H = \frac{\hbar}{4}\omega_0 \sigma \cdot \tau - \frac{\hbar}{2}\omega_\mu \sigma_z + \frac{\hbar}{2}\omega_e \tau_z \tag{2.13}$$

where $\omega_0 = 2\pi A$, and σ and τ are the Pauli matrices.

In table 2.3, where the $|m_\mu\, m_e\rangle$ set has been used as a base of the spin space we can find the eigenvectors and respective eigenvalues for hamiltonian 2.3. We can define, for simplicity, a characteristic field B_0 ($B_0 = 0.1585$ T in vacuum) and a reduced field x as:

$$B_0 = \frac{A}{\gamma_e + \gamma_\mu} \tag{2.14}$$

$$x = \frac{B}{B_0} \tag{2.15}$$

and the amplitudes of probability are:

$$\begin{aligned} \cos\zeta &= \left(\frac{1 + \frac{1}{2}\left(\frac{B_0}{B}\right)^2}{1 + \left(\frac{B_0}{B}\right)^2} \right)^{\frac{1}{2}} = \left(\frac{2x^2+1}{2(x^2+1)} \right)^{\frac{1}{2}} \\ \sin\zeta &= \left(\frac{\frac{1}{2}\left(\frac{B_0}{B}\right)^2}{1 + \left(\frac{B_0}{B}\right)^2} \right)^{\frac{1}{2}} = \left(\frac{1}{2(x^2+1)} \right)^{\frac{1}{2}} \end{aligned} \tag{2.16}$$

Table 2.3: Isotropic muonium eigenvectors and eigenvalues corresponding to the Breit-Rabi hamiltonian 2.3. B_0 and the amplitudes of probability $\cos\zeta$ and $\sin\zeta$ are defined in equations 2.14 and 2.16 [6].

Eigenstate	Eigenvectors (base $\|m_\mu\, m_e\rangle$)	Eigenenergy
$\|1\rangle$	$\|++\rangle$	$\frac{h\,A}{4} + \frac{h(\gamma_e-\gamma_\mu)\,B}{2}$
$\|2\rangle$	$\sin\zeta\|+-\rangle + \cos\zeta\|-+\rangle$	$-\frac{h\,A}{4} + \frac{h(\gamma_e+\gamma_\mu)\sqrt{B^2+B_0^2}}{2}$
$\|3\rangle$	$\|--\rangle$	$\frac{h\,A}{4} - \frac{h(\gamma_e-\gamma_\mu)\,B}{2}$
$\|4\rangle$	$\cos\zeta\|+-\rangle - \sin\zeta\|-+\rangle$	$-\frac{h\,A}{4} - \frac{h(\gamma_e+\gamma_\mu)\sqrt{B^2+B_0^2}}{2}$

Breit and Rabi [51] were the first to consider the effect of an applied magnetic field on hyperfine levels. The corresponding diagram of the hyperfine energy levels as a function of the applied magnetic field B is therefore usually known as the Breit-Rabi diagram. To better comprehend the essential physics contained in table 2.3 we will consider the asymptotic limits $B = 0$ and $B \to \infty$ [6]. In the asymptotic limit $B = 0$ (or in the limit of small magnetic fields $B << B_0$), the two spins add up to a total spin F=1, yielding a triplet $F = 1$ state with energy $h\,A/4$

$$|1\rangle = |++\rangle = |F=1, m_F=+1\rangle \tag{2.17}$$

$$|2\rangle = \frac{\sqrt{2}}{2}|+-\rangle + \frac{\sqrt{2}}{2}|-+\rangle = |F=1, m_F=0\rangle \tag{2.18}$$

$$|3\rangle = |--\rangle = |F=1, m_F=-1\rangle \tag{2.19}$$

and a singlet $F = 0$ state with energy $-3\,h\,A/4$

$$|4\rangle = \frac{\sqrt{2}}{2}|+-\rangle - \frac{\sqrt{2}}{2}|-+\rangle = |F=0, m_F=0\rangle \tag{2.20}$$

In the high magnetic field limit $B >> B_0$, the muon and the electron spins are decoupled and each then has the two Zeeman levels in the presence of the magnetic field B:

$$|1\rangle \rightarrow |++\rangle \tag{2.21}$$
$$|2\rangle \rightarrow |-+\rangle \tag{2.22}$$
$$|3\rangle \rightarrow |--\rangle \tag{2.23}$$
$$|4\rangle \rightarrow |+-\rangle \tag{2.24}$$

In the case where $A = 0$ (or in the limit of $\mu_B\, B >> h\, A$), the two spins are basically free, and each then has two energy levels in the presence of the magnetic field B, separated by the Larmor energy $\mu_B\, B$.

Because the problem of muonium formation in matter is essentially one of statistical physics of quantum systems, it is best dealt with by the density-matrix, $\rho(t)$, formalism [52]. The quantity of interest is essentially the polarization $\vec{p_\mu}(t)$ of the muon spin ensemble, which arises from the known result [52]:

$$\vec{p_\mu}(t) = Tr[\rho(t)\vec{\sigma}_\mu] \tag{2.25}$$

where the density-matrix is defined as

$$\rho(t) = \frac{1}{4}\left[1 + \vec{p_\mu}(t)\cdot\vec{\sigma}_\mu + \vec{p_e}(t)\cdot\vec{\sigma}_e + \sum_{jk} P^{jk}(t)\sigma_\mu^j\sigma_e^k\right] \tag{2.26}$$

Attending to the usual initial condition arising from muonium being formed statistically with 50% electron spin up and 50% electron spin down:

$$\rho(0) = \frac{1}{4}\left[1 + \vec{p_\mu}(0)\cdot\vec{\sigma}_\mu\right] \tag{2.27}$$

The time dependent muon spin polarization projection in the muon in-

coming direction can then be proved to correspond to a sum of muonium frequencies

$$p_\mu(t) = \sum_{\mathrm{nm}} a_{\mathrm{nm}} \cos 2\pi\nu_{\mathrm{nm}} t \tag{2.28}$$

where the precession amplitudes a_{nm} and frequencies $\nu_{\mathrm{nm}} = (E_{\mathrm{n}} - E_{\mathrm{m}})/h$ are summarized in table 2.4. The $1-3$ and $2-4$ transitions correspond to forbidden transitions and are not observed [50].

Table 2.4: Isotropic muonium precession amplitudes and frequencies.

nm	a_{nm}	$\nu_{\mathrm{nm}} = \lvert E_{\mathrm{n}} - E_{\mathrm{m}}\rvert/h$
12	$(\cos\zeta)^2/2$	$\left\lvert \frac{A}{2} + \frac{(\gamma_e-\gamma_\mu)\,B}{2} - \frac{(\gamma_e+\gamma_\mu)\sqrt{B^2+B_0^2}}{2} \right\rvert$
34	$(\cos\zeta)^2/2$	$\left\lvert \frac{A}{2} - \frac{(\gamma_e-\gamma_\mu)\,B}{2} + \frac{(\gamma_e+\gamma_\mu)\sqrt{B^2+B_0^2}}{2} \right\rvert$
14	$(\sin\zeta)^2/2$	$\left\lvert \frac{A}{2} + \frac{(\gamma_e-\gamma_\mu)\,B}{2} + \frac{(\gamma_e+\gamma_\mu)\sqrt{B^2+B_0^2}}{2} \right\rvert$
23	$(\sin\zeta)^2/2$	$\left\lvert -\frac{A}{2} + \frac{(\gamma_e-\gamma_\mu)\,B}{2} + \frac{(\gamma_e+\gamma_\mu)\sqrt{B^2+B_0^2}}{2} \right\rvert$

Again, much insight arises from inspection of the asymptotic limits [6]. In the low-field limit ($B << B_0$), one has

$$\nu_{12} \rightarrow \frac{(\gamma_e - \gamma_\mu)\,B}{2} \tag{2.29}$$

$$\nu_{14} \rightarrow A \tag{2.30}$$

$$\nu_{23} \rightarrow \frac{(\gamma_e - \gamma_\mu)\,B}{2} \tag{2.31}$$

$$\nu_{34} \rightarrow A \tag{2.32}$$

For usual vacuum-like values of the hyperfine interaction (the GHz range) ν_{14} and ν_{34} fall out of experimentally accessible range. Only the ν_{12} and ν_{23} of the muonium precession frequencies are therfore accessible experimentally: these frequencies coincide at low fields, and are here independent of the hyperfine interaction, simply corresponding to a gyromagnetic ratio of 1.4×10^4 MHz/T. Measurements at low fields are therefore most useful to identify the presence of muonium, but nothing can be extracted about the hyperfine interaction.

In the high-field limit, we have

$$\nu_{12} \rightarrow \gamma_\mu B - \frac{A}{2} \tag{2.33}$$

$$\nu_{14} \rightarrow \gamma_e B + \frac{A}{2} \tag{2.34}$$

$$\nu_{23} \rightarrow \gamma_e B - \frac{A}{2} \tag{2.35}$$

$$\nu_{34} \rightarrow \gamma_\mu B + \frac{A}{2} \tag{2.36}$$

In this case, the higher ν_{14} and ν_{23} frequencies are generally unobservable, and the lower ν_{12} and the ν_{34} frequencies are symmetrically placed around the diamagnetic line at $\gamma_\mu B$, the difference between them being a direct measurement of the hyperfine interaction A.

Figures 2.1, 2.2, and 2.3 illustrate the field-dependence of the energy levels, precession frequencies and precession amplitudes, respectively.

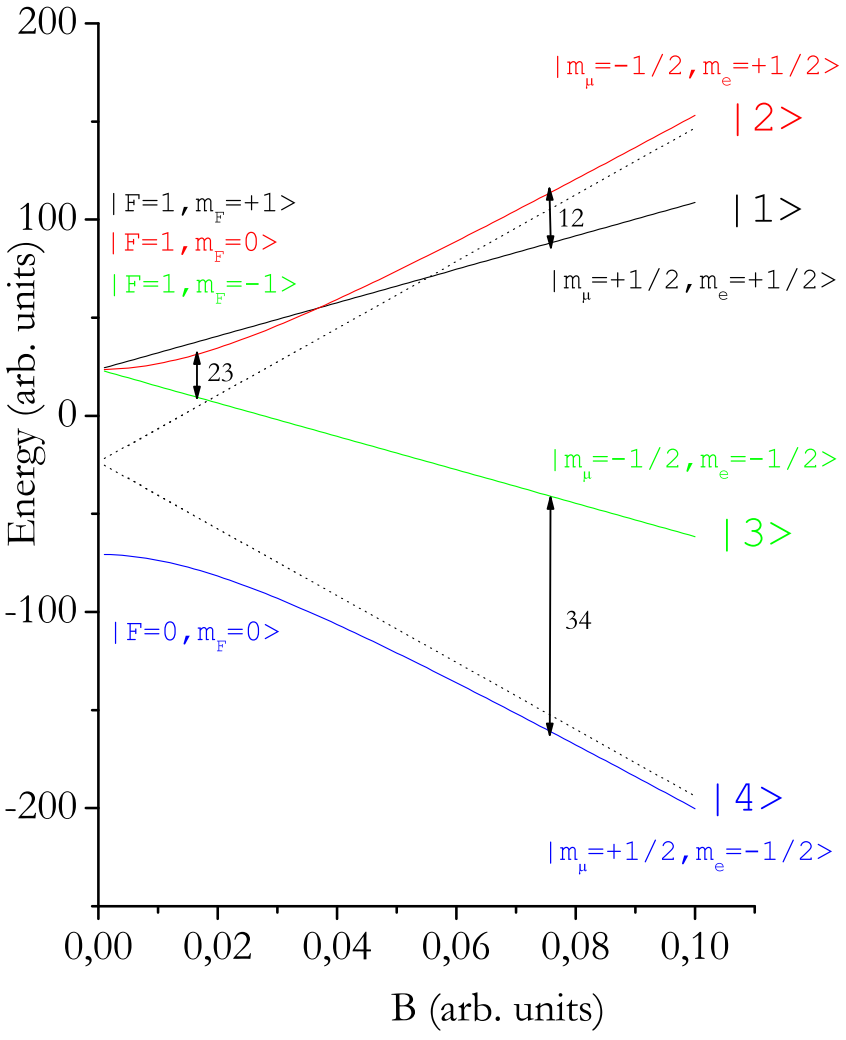

Figure 2.1: Energy eigenvalues of the isotropic muonium hyperfine hamiltonian 2.3, as a function of the applied magnetic field B. This diagram is usually known as the Breit-Rabi diagram. A fictitious value of γ_e ($\gamma_e = 3\gamma_\mu$) was used, in order to display more clearly the essential features of this diagram. The asymptotes of the non-linear eigenenergies of the $|2\rangle$ and $|4\rangle$ eigenstates are drawn as well (dashed lines).

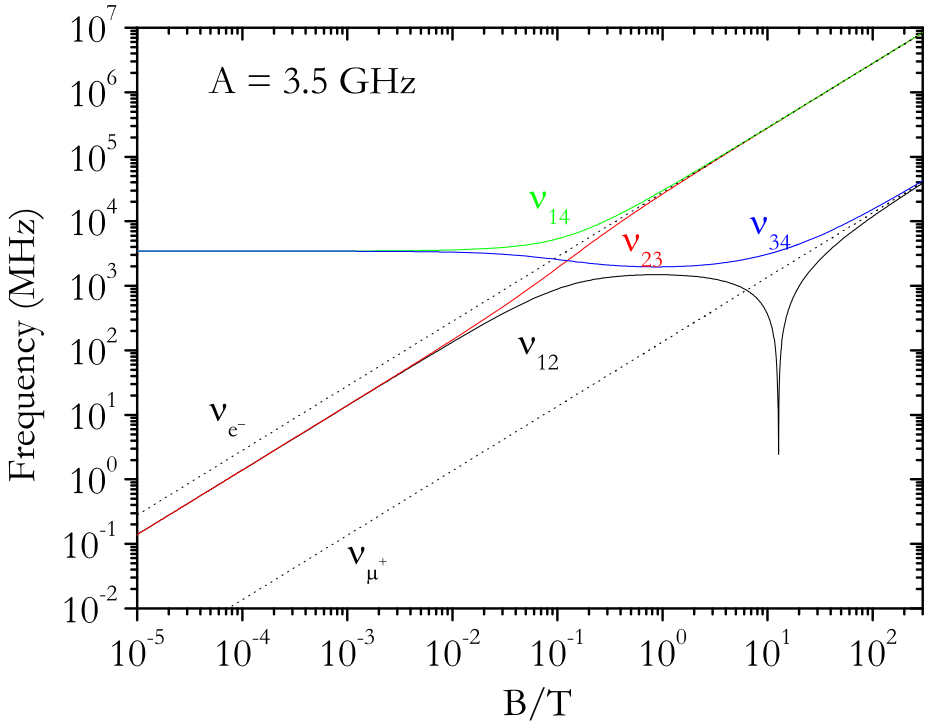

Figure 2.2: Hyperfine transition frequencies for an isotropic muonium state with $A = 3.5$ GHz, as a function of the applied magnetic field B. The Larmor precession frequencies of the free muon and the free electron are drawn as dashed lines, clearly showing that for high fields the ν_{14} and the ν_{23} frequencies tend to $\nu_e \pm A/2$ and that the ν_{12} and the ν_{34} frequencies tend to $\nu_\mu \pm A/2$. The latter is preceded by the $1-2$ level crossing at 12.7 T.

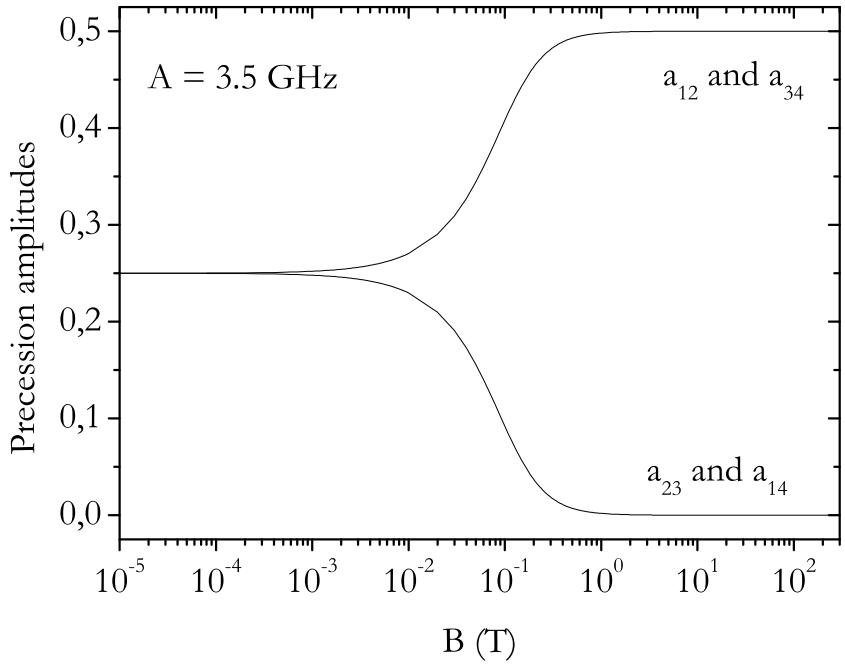

Figure 2.3: Amplitude of the permitted hyperfine transitions for isotropic muonium with $A = 3.5$ GHz, as a function of the applied magnetic field B. The spectral weight is seen to be transferred at high fields from the $2-3$ and $1-4$ transitions to the $1-2$ and $3-4$ transitions.

2.2.2 Anisotropic "anomalous" muonium

The above formalism may be easily extended to the case where the electronic wavefunction is not isotropic, as in the bond-centred state found in silicon. The hyperfine interaction parameter now becomes a 2^{nd}–rank hyperfine tensor and the hamiltonian writes (using as bases equation 2.13):

$$H = \frac{\hbar}{4}\omega_0 \sigma \cdot \tau + \frac{\hbar}{4}\omega^*(\sigma \cdot n)(\tau \cdot n) - \frac{\hbar}{2}\omega_\mu \sigma_z + \frac{\hbar}{2}\omega_e \tau_z \qquad (2.37)$$

defining now $\omega_0 = 2\pi A_\perp$, and $\omega^* = 2\pi(A_\parallel - A_\perp)$ where $A_\perp$ and $A_\parallel$ are the perpendicular and parallel components of the tensor can be expressed in terms of an isotropic component A_{iso} and a dipolar component D as [53]:

$$A_{\perp} = A_{\text{iso}} + D \tag{2.38}$$

$$A_{\parallel} = A_{\text{iso}} - 2\,D \tag{2.39}$$

Though it is possible to express analytically the eigenenergies and eigenvectors of the hamiltonian 2.37 for some important particular cases [50], the general solution can only be obtained numerically. As can easily be anticipated, the precession amplitudes and frequencies are now dependent not only of the applied magnetic field $\boldsymbol{B}$, but also from the angle between $\boldsymbol{B}$ and the symmetry axis of the hyperfine center. We shall however go no further in the description of this particularly important model, since no direct experimental signs of anisotropic muonium were obtained in this investigation. For further developments, see the "classical" references [50, 53].

2.2.3 Quenching of isotropic muonium polarization in a magnetic field

The existence of muonium dynamical processes pre– or post–thermalization may lead to significant depolarization of the muon spin. In such cases, it is usual to quench the muon polarization by application of an external magnetic field parallel to the initial muon spin. Such longitudinal field quenching experiments allow much insight into the strength of the depolarization mechanism. In these experiments, the polarization decay may be observed in the time spectrum as a polarization relaxation, thus providing access to the depolarization rates. Such longitudinal-field studies are therefore usually designated by muon-spin-relaxation studies.

The theoretical framework for isotropic muonium subject to no dynamical depolarization process is now presented, since it is the most fundamental front in these studies.

As seen before, in the process of muonium formation, the muon captures an electron, forming, in the spin sub-space $|m_{\mu}, m_e\rangle$, one of the initial states $|+,+\rangle$, $|+,-\rangle$, $|-,+\rangle$ or $|-,-\rangle$. As can be seen in table 2.3, in the absence of any applied field (i.e., in zero-field), the states $|+,+\rangle$ and $|-,-\rangle$ are

eigenstates of the Breit-Rabi hamiltonian and therefore stationary, whereas the states $|-,+\rangle$ and $|+,-\rangle$ are superpositions of the $^1S_0$ and $^3S_1$, $m_F = 0$, $|2\rangle$ and $|4\rangle$ states. For typical values of A, these muonium atoms formed in the latter non stationary states will therefore oscillate with the hyperfine frequency between the $|2\rangle$ and $|4\rangle$ states and depolarize too quickly to be observed. Thus the observable polarization is only 50%. In the high-field Paschen-Back *régime*, the initial states will all correspond to eigenstates, and therefore the polarization will be preserved.

The characteristic variation of the polarization with an applied longitudinal field can therefore probe the formation of muonium. The correspondent time – and field – dependent polarization is found to be, for isotropic muonium [50]:

$$p(t) = a_{\parallel} + \frac{(\sin 2\zeta)^2}{2} \cos 2\pi\nu_{24} t \tag{2.40}$$

where

$$a_{\parallel} = (\cos 2\zeta)^2 + \frac{(\sin 2\zeta)^2}{2} \tag{2.41}$$

and the frequency ν_{24} is, from the values of table 2.3.

$$\nu_{24} = (\gamma_\mu + \gamma_e)\sqrt{B^2 + B_0^2} \tag{2.42}$$

ν_{24} is in general too high to be experimentally visible and the corresponding parcel in equation 2.40 thus simply averages out to zero, yielding the polarization curve:

$$p = a_{\parallel} = \frac{1}{2} + \frac{x^2}{2\,(1+x^2)} \tag{2.43}$$

An example is shown in Fig.2.4 where $A = 3.5(1)$GHz is the fitted value of the hyperfine interaction we have a fraction of 40% of muonium present. For low fields, as discussed in the preceding section, half of the of that fraction, 20%, is lost, and at high fields the muonium states formed correspond to eigenvectores and are therefore stationary, the muon spin polarization being preserved. This curve is known as repolarization curve.

This method can constitute a very powerful tool to probe the formation of muonium, even in cases where muonium is subject to strong dynamical interactions that lead to the loss of muon spin polarization, thus preventing its direct spectroscopical identification. This loss in muon spin polarization is often designated "missing fraction".

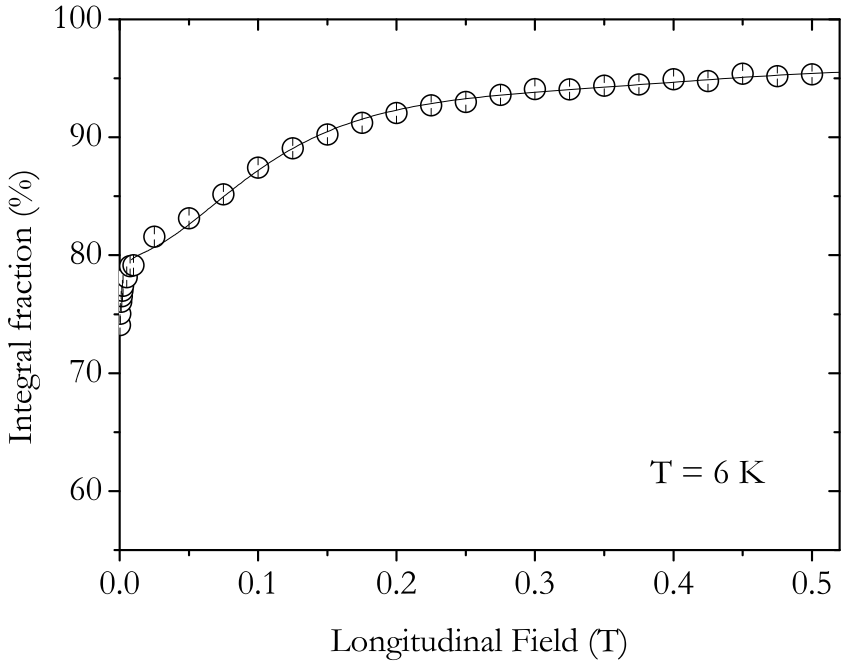

Figure 2.4: Dependence of the muon spin polarization with the applied longitudinal magnetic field B, for TeO_2 at T=6 K an isotropic muonium state with $A = 3.5(1)$GHz. The spin polarization is shown to vary from 73% at zero-field up to 96% at high-fields. This curve is therefore known as a repolarization curve. A low-field deviation to the repolarization curve is observed, which will be discussed in Chapter 4.

2.2.4 Muonium dynamics

When dynamical processes such as charge or spin–exchange exist, they can induce a depolarization of the muon spin. This simply arises due to the

finite lifetime of the converting state, as can be seen from the following very simple argument. If a state 1 is converting to a state 2 with a rate $\lambda = 1/\tau$, where τ is the lifetime of state 1:

$$Mu_1 \underset{\lambda}{\rightarrow} Mu_2 \tag{2.44}$$

then the polarization change dP_1 of state 1 in a time interval dt will be

$$dP_1 = -\lambda\, P_1\, dt \tag{2.45}$$

implying an exponential relaxation of the corresponding polarization

$$P_1(t) = P_1^0\, \exp(-\lambda\, t) \tag{2.46}$$

It is possible to have access to these conversion and/or inter-conversion processes if λ is inside the experimental frequency window, which appear *via* relaxation of the corresponding states' polarization. If λ is too high, then the entire polarization of the converting state is lost before it can be observed and a "missing fraction" in the polarization is detected. In such conversion cases, the precession frequency of the final state can nevertheless be observed and the existence of a prior conversion process can be inferred from the shifting of the precession phase.

The general form of the polarization of muonium subject to interconversion dynamical processes can then be written as a sum of exponentially relaxing phase-shifted precession frequencies [50]:

$$P(t) = \sum_{nm} a_{nm} \exp\left(-\lambda_{nm}\, t\right) \cos\left(2\pi\nu_{nm} t + \phi_{nm}\right) \tag{2.47}$$

Muonium dynamics has been the object of intensive theoretical treatment over the years [50]. We shall not discuss it extensively here since it does not constitute the essential objective of this work.

2.3 Production of polarized muon beams and muon decay

The basic production of positive muons is schematically represented in Figure 2.5. High energy-protons (500MeV) are directed to a carbon or beryllium target, where positive pions are produced in the reaction:

$$p + p \rightarrow \pi^+ + ... \tag{2.48}$$

The positive pions decay within 26ns to a positive muon and a muon neutrino.

$$\pi^+ \xrightarrow[2.6\,ns]{} \mu^+ + \nu_\mu \tag{2.49}$$

Since neutrinos always have their spins antiparallel to their linear momentum (negative helicity), the positive muons arising from pions decaying at rest in the target also have their spins antiparallel to their momentum. This allows to obtain a nearly 100% spin-polarized muon beam from pion decaying at the target.

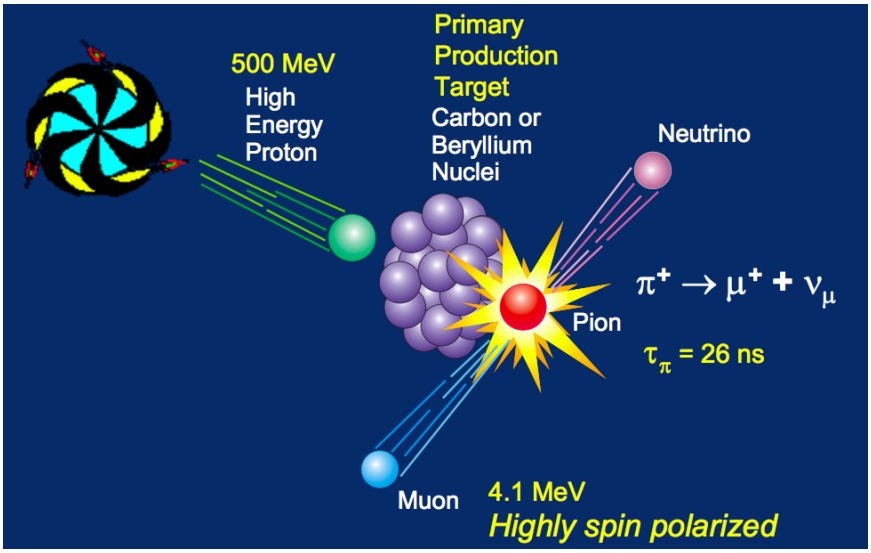

Figure 2.5: Simple scheme on production of positive muons using a cyclotron [3]

Muons are radioactive particles, decaying *via* weak interaction with a meanlife of 2.2 μs, according to equation:

$$\mu^+ \xrightarrow[2.2\,\mu s]{} e^+ + \nu_e + \nu_\mu \tag{2.50}$$

The usefulness of the spin-polarized muon as a condensed matter probe comes from the decay reaction of the muon (eq. 2.50). In the muon's reference frame, the positron is emitted with a maximum kinetic energy $E_{\max} = 52.3$ MeV. Governed by the weak interaction, the muon decay does not follow parity conservation, and this shows up as an asymmetry in the positron emission direction. The probability dW for emission of a positron with energy in the interval $[E, E + dE]$, in the directions inside the cone with aperture angle between $[\theta, \theta + d\theta]$ (defined with respect to the direction of the muon's spin), is defined by the expression:

$$dW = \frac{G^2 m_\mu^5}{192\pi^3} (3 - 2\varepsilon)\, \varepsilon^2 \left[1 + A(\varepsilon) \cos\theta\right] d\varepsilon\, d\cos\theta \tag{2.51}$$

where $G/\sqrt{2} = 1.01 \times 10^{-5} m_p^{-2}$ expresses the intensity of the weak interaction (m_p is the proton's mass), $\varepsilon = E/E_{\max}$ is the energy of the positron normalized to the maximum energy and $A(\varepsilon)$ is a factor governing the asymmetry in the angular distribution of the decay positrons.

$$A(\varepsilon) = \frac{2\varepsilon - 1}{3 - 2\varepsilon} \tag{2.52}$$

The angular distribution of decay positrons is represented in Fig. 2.6 for some values of the asymmetry factor, as well as for the average asymmetry value, $\langle a \rangle$, for all energies $\left(\langle a \rangle = \frac{1}{3}\right)$.

These characteristics of the muon decay allow the monitoring of the muon spin direction, after implantation in a material, by measuring the time evolution of the asymmetry in the positron emission. Of course, a *sine qua non* condition for that is the presence of some degree of spin polarization of the ensemble of implanted muons (*i.e.*, a non-zero average component in some direction of the ensemble of muon spins).

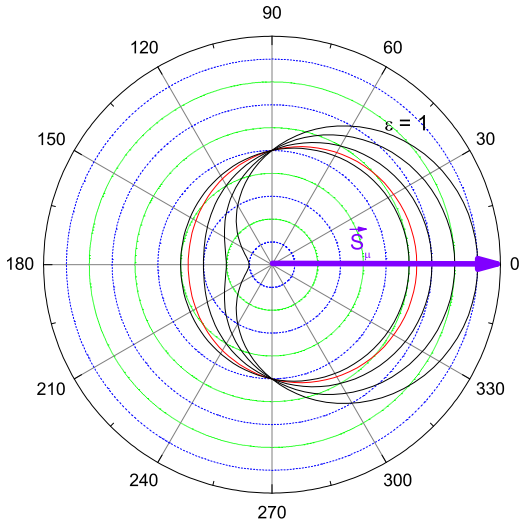

Figure 2.6: Angular distribution of decay positrons with relation to the muon spin direction (at 0 degrees). We represent the cases of maximum positron energy, as well as the result of integration over all energies (red line).

2.4 Muon spin rotation, relaxation, resonance

2.4.1 Basic experimental setup

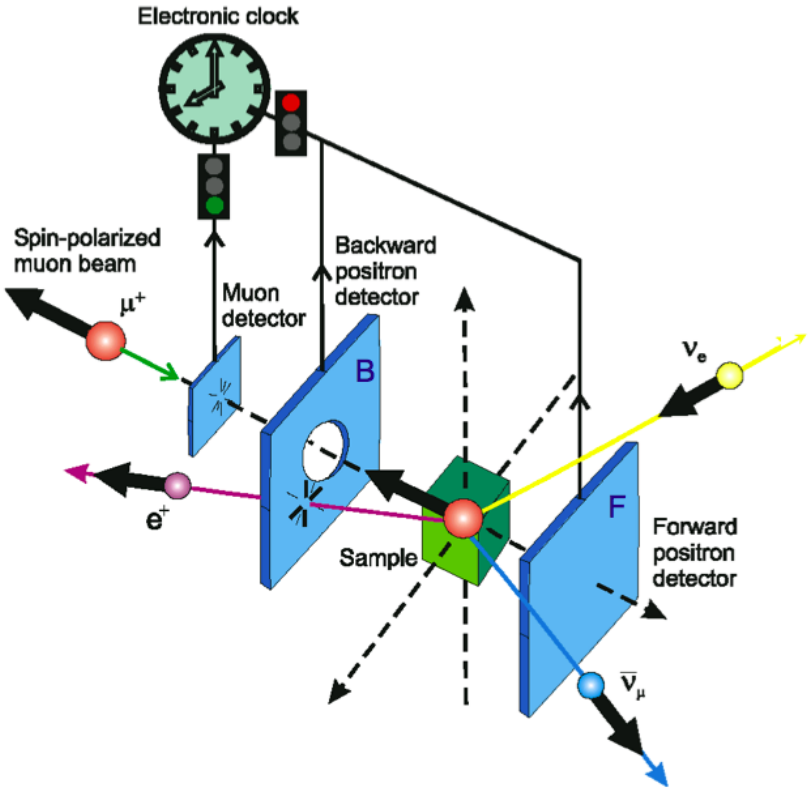

Figure 2.7: Simple scheme on μSR experimental setup [3]

In Fig. 2.7 we find the basic experimental setup for muon experiments. The spin-polarized muon beam is directed towards a sample of the material under scrutiny. A minimum of two positron detectors is adequately placed around the sample, usually in the forward (F) and backward (B) positions with respect to the upcoming beam. The basic sample environment includes adequate instruments for temperature dependence studies (cryostats, furnaces). External magnetic fields may be applied to the sample region, as will be detailed in the following sections.

The number of counts N_D in detector D may be described by the expres-

sion:

$$N_D = B_D + N_0 \varepsilon_D \left[1 \pm A\, P_z\left(t\right)\right] \exp\left(-\frac{t}{\tau_\mu}\right) \tag{2.53}$$

where:

- B_D is a factor describing the spurious (background) counts in the detector, which in principle are time-independent;
- N_0, multiplied by the number of detectors, corresponds to the number of real events at time zero;
- ε_D is the detection efficiency, relating not only to the detector intrinsic efficiency, but also to the geometrical disposition (for example, a detector placed farther away detects less positrons, thus decreasing ε;
- A is the intrinsic asymmetry of the detector arrangement. For detector B, the count rate is proportional to $(1 + A)$, in the case of fully polarized muons with polarization in the detector's symmetry axis; in the same circumstances, the count rate is proportional to $(1 - A)$ for detector F;
- $P_z\left(t\right)$ is the time evolution of the z component of the muon spin polarization (where the z axis is defined by the incoming beam direction);
- τ_μ is the muon lifetime;

The main objective of these experiments is obtaining $P_z(t)$. This is usually done in two steps: by obtaining (i) the asymmetry $A\, P_z(t)$ in the experiment *proper* and (ii) the intrinsic detector asymmetry A in calibration measurements.

The intrinsic asymmetry A is in general less than the maximum theoretical value of 1/3 [53]. It is normaly determined by calibration measurements on a sample where the muon spin polarization is known. Silver is usually used for this purpose, because 100% of the muons implanted on this metal are known to form an easily identifiable non-relaxing diamagnetic fraction.

Low-transverse field (20 G) measurements on Ag are thus commonly used for these calibrations.

The experimental asymmetry is obtained through the difference between the number of counts in detectors F and B (after subtracting the background counts), normalized to the total number of counts (for more complex detector dispositions, simple generalizations apply):

$$A_{\text{exp}}(t) = \frac{[N_B(t) - B_B] - [N_F(t) - B_F]}{[N_B(t) - B_B] + [N_F(t) - B_F]} \tag{2.54}$$

However, due to different detector efficiencies, the expression 2.54 does not give us $A\,P_z(t)$ directly, but instead (after considering eq. 2.53):

$$A_{\text{exp}}(t) = \frac{(\alpha - 1) + (1 + \alpha)\,A\,P_z(t)}{(1 + \alpha) + (\alpha - 1)\,A\,P_z(t)} \tag{2.55}$$

where

$$\alpha = \frac{\varepsilon_B}{\varepsilon_F} \tag{2.56}$$

It is therefore necessary to correct the experimental asymmetry 2.54, which is usually done by computing:

$$A_{\text{corr}}(t) = \frac{N_B(t) - \alpha N_F(t)}{N_B(t) + \alpha N_F(t)} = A\,P_z(t) \tag{2.57}$$

The quantity α depends both on the intrinsic detection of the detectors and the geometrical details of the experimental setup, including positron absorption factors such as the sample thickness and the cryostat walls. α must therefore be determined for each case, usually together with the calibration measurements for the intrinsic (maximum) asymmetry A.

2.4.2 Muon spin rotation

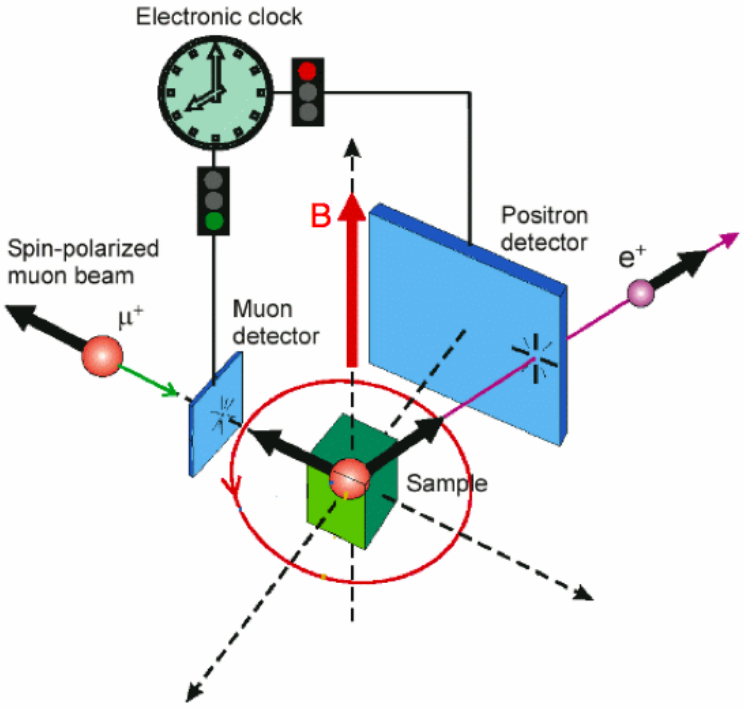

Figure 2.8: Simple scheme of the muon spin rotation experimental setup [3]

Figure 2.8 illustrates the simplest experimental geometry, witch corresponds to the case where an external magnetic field B is applied perpendicularly to the initial muon spin polarization. With this configuration, and in the situation where the muon spin is subject only to the Zeeman interaction (the simplest situation) with the applied magnetic field, a simple precession of the spin occurs around B, with the Larmor frequency ν_L:

$$\nu_L = \gamma_\mu B \tag{2.58}$$

In this case, the polarization component in the initial direction z has a sinusoidal temporal evolution:

$$P_z(t) = P_{\max} \cos(2\pi\nu_L t + \phi) \tag{2.59}$$

where the phase ϕ depends on the definition of time zero $t = 0$, and is trivially associated with precession frequencies high enough (compared with the experimental resolution) for a non-negligible rotation of the polarization to occur between the initial cintilator and the sample. These trivial phase shifts present no temperature dependence and are simply proportional to the applied field. The existence of a temperature-dependent phase-shift is a clear sign of conversion between states, but those studies were not done in this work and so are beyond the scope of this thesis.

This subtechnique is based upon the characteristic precession frequencies of the muon spin in the presence of the hyperfine field, due to the hyperfine interaction between the muon spin and the electron spin. These precession frequencies of the muon present a distinctive behaviour with an applied magnetic field, as we move from the Zeeman *régime* where the hyperfine field dominates, to the Paschen-Back *régime* where the applied field is preponderant. Such studies, based upon the precession (or rotation) of the muon spin, are also designated muon spin rotation studies.

Despite the pure hyperfine frequency being observable in zero-field, the observation of the characteristic applied-field-dependence of the muonium precession frequencies requires that the applied field has a component perpendicular to the muon spin. Such spectroscopic studies are therefore best done in the transverse field geometry, where the external magnetic field is applied perpendicularly to the muon initial spin polarization

In Fig. 2.9 we show a particularly simple example, for calibration measurements on a silver sample. The individual time histograms for detectors F and B are shown, together with the corresponding asymmetry. The geometrical factor α can be extracted from these type of measurements as follows: the different detection efficiencies originating $\alpha \neq 1$ imply, in these TF measurements, that the experimental asymmetry oscilates with time around an average value different from zero. Fits to the time spectra are performed after correction of this offset by the fitting routine.

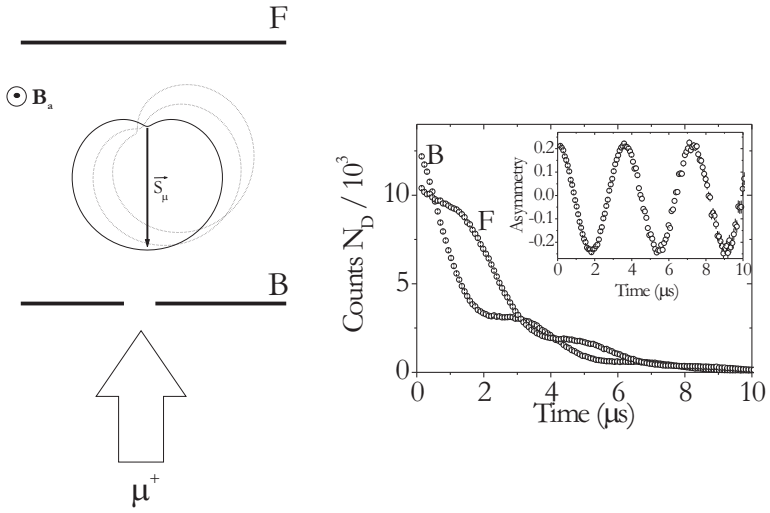

Figure 2.9: The basic muon spin rotation experiment. In the left side we sketch the basic setup: spin-polarized positive muons are implanted into a sample, in a region subjected to a magnetic field B_a perpendicular to the initial muon spin, surrounded by two positron detectors in the forward (F) and backward (B) direction. The asymmetric probability for positron emission rotates with the muon spin and is drawn for three different times. The positrons are detected by detectors F and B, forming histograms like those shown in the right side. The corrected asymmetry $A_{\rm corr}(t) = (N_B - \alpha N_F)/(N_B + \alpha N_F)$ is shown as an inset.

In muon spin rotation measurements, the presence of paramagnetic muonium is easily identified by its characteristics precession frequencies. A typical experimental test for the presence of paramagnetic muonium is done at low-field, where the characteristic $\nu_{12} = \nu_{23}$ precession at 1.4×10^4 MHz/G is observed. An example is shown in figure 2.10.

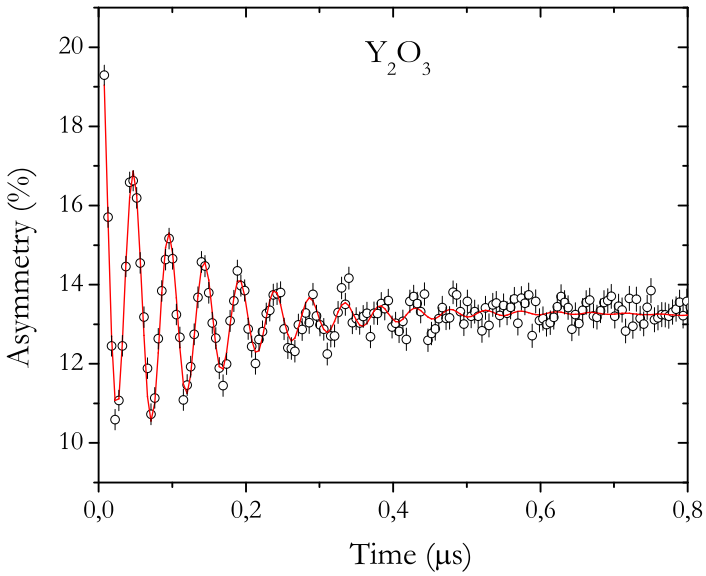

Figure 2.10: Time spectrum of a Y_2O_3 sample at T=300 K and transverse field B=15 mT. The characteristic muonium $\nu_{12} = \nu_{23}$ precession at 21 MHz is observed. This precession frequency allows us to verify the presence of muonium, but it is not adequate for its characterization, since it is independent of the hyperfine interaction. In this particular example, the muonium precession is seen to be heavily damped, which is a clear sign of muonium dynamical behavior.

2.4.3 Muon spin relaxation

For relaxation studies longitudinal geometry is used (Fig. 2.7), by applying an external magnetic field parallel to initial polarization. In this case, the alterations to polarization arise from muon spin-flips in the presence of the magnetic field, by interactions with the lattice. As was discussed in section 2.2.4 such spin-flipping motivate a gradual loss of polarization, generally visible via a relaxation in asymmetry. The geometrical parameter α may eventually change with the magnitude of the applied field, in these measurements, due to the alteration of the positron trajectories, particularly

for high-fields, where the charged particles trajectories may be significantly changed. In these cases, it may be necessary to perform a silver calibration in the entire field range.

As mentioned as well in section 2.2.4, and will be shown in the forthcoming chapters, such longitudinal field measurements also prove much useful for the investigation of the strength of depolarizing mechanisms *via* quenching of the muon spin polarization.

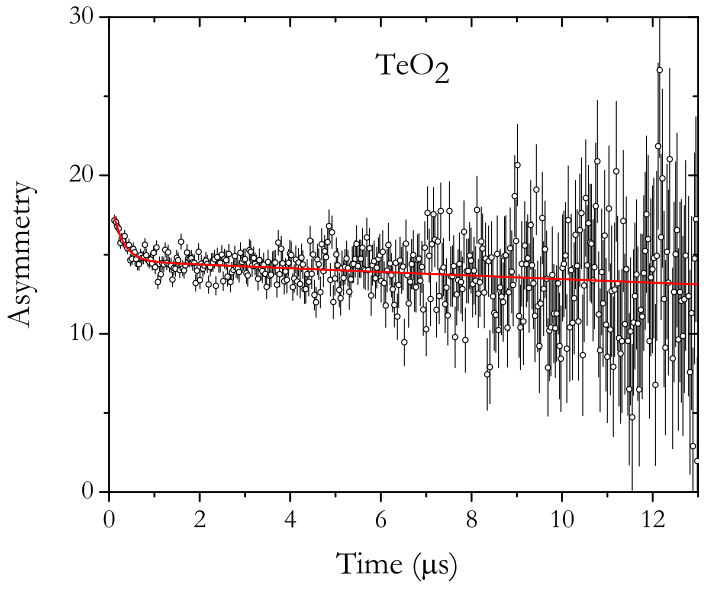

Figure 2.11: Time spectrum of a TeO_2 sample at T=300 K, subject to a longitudinal field of B=2 G. The appearance of a relaxation in this nuclear-magnetic-moment-free compound is a sign of dynamical processes envolving the muonium states.

2.4.4 Muon spin resonance

The occurrence of muon spin depolarization in the muon thermalization process and/or the existence of muon charge/spin dynamics may lead to a "missing fraction" in the polarization, as seen in transverse- or longitudinal-field measurements, thus hiding the nature of the final state. However, if a

given state is present, albeit depolarized, its presence may be demonstrated by a change in the longitudinal field polarization induced by forcing transitions between the corresponding spin levels, by means of resonant electromagnetic radiation.

In this *muon-spin resonance* method, one basically begins with a longitudinal-field configuration, and then forces the transitions between the spin energy-levels in the presence of the static longitudinal field, by means of electromagnetic radiation.

However, this being not the focal sub-technique used in this work, we will not go further in its details, which can be found elsewhere [17]

2.4.5 User facilities and spectrometers

The muon production process requires a proton accelerator capable of reaching hundreds of MeVs. Such accelerators exist only in large-scale installations. Currently, the following muon user facilities exist in four laboratories around the world:

- ISIS pulsed muon facility at the Rutherford Appleton Laboratory, in the United Kingdom;
- Laboratory for muon spin spectroscopy at the Paul Scherrer Institut, in Switzerland;
- Centre for molecular and materials science at the Tri-University Meson Facility (TRIUMF), in Canada;
- J-PARC Muon Facility at J-PARC Materials and Life Science Experimental Facility, in Japan.

In this work, we have used the spectrometers EMU at ISIS, and GPS and DOLLY at PSI. Each has particular characteristics and capabilities.

In short, the specific advantages of each facility may be summarized as follows: high resolution spectroscopic measurements are possible at PSI, which also has a versatile furnace setup. ISIS, as a pulsed source, can not compete with such high resolutions, but the existence of pulsed radio-frequency

capabilities from liquid-helium temperatures up to much above room temperature (c. 1300 K), allows deeper research by RF-μSR final-state analysis of diamagnetic states.

Chapter 3

Experimental Results and Discussion

3.1 Sample and experimental details

In the experiments, a monocrystalline α-TeO_2 sample (obtained commercially from the MTI corporation) was used. The implanted muon spin polarization was parallel to the 100 axis. Conventional transverse-field, longitudinal-field and radio frequency measurements were undertaken from liquid-helium temperature up to room temperature, and the respective experimental details are presented in this chapter. In order to reduce the spurious (background) events, both the flypast setup at ISIS [54] and the veto detector at PSI [55] were used. The sample was stored and handled in air. During the measurements, the sample was in low-pressure helium exchange gas. No significant change with ambient atmosphere is expected to occur for temperatures below 650K [41]. Although no information is available about the concentration of dopants in the sample, we note that usual commercial samples of TeO_2 are expected to present aliovalent impurity concentrations of about 0.1 ppm, [56] which are too low in order to expect any direct interaction with the implanted muon.

3.2 Raw Data Analysis

In this section we will take some time describing the methods used to analysis the raw data obtained from the conventional transverse-field, longitudinal-field and radio frequency measurements. For this analysis the WiMDA [57] program was used.

3.2.1 Transverse-Field Analysis

We begin by showing two typical time spectra for a 1.5 mT applied field at two different temperatures 300K and 5K (Fig. 3.1)

At both temperatures we can clearly see a slightly damped oscillation at the Larmor frequency of 0.204 MHz (Eq. 3.1) corresponding to muons in a diamagnetic environment.

$$\frac{\omega}{2\pi} = \frac{\gamma\mu B}{2\pi} = 0.204\text{MHz} \tag{3.1}$$

In addition, a strong relaxation is present in the first few hundred nanoseconds, which we assign to muons in a paramagnetic environment, as discussed below. We have fitted the time spectra with the sum of two components:

$$A(t) = A_{\text{slow}} e^{-\lambda_{\text{slow}} t} cos(\omega t + \phi_{slow}) + A_{\text{fast}} e^{-\lambda_{\text{fast}} t} \tag{3.2}$$

An oscillating and a non-oscillating part, both with an exponential damping, where the subscripts "slow" and "fast" stand for the slowly relaxing and the fast relaxing component, respectively. Some spectra were also analyzed with different damping functions for the fast relaxing component as described in the text. Note that the "fast" decay is so fast that Eq. 3.2 is indistinguishable, for a temperature dependence, from

$$A(t) = \left[A_{\text{slow}} e^{-\lambda_{\text{slow}} t} + A_{\text{fast}} e^{-\lambda_{\text{fast}} t}\right] cos(\omega t + \phi_{slow}) \tag{3.3}$$

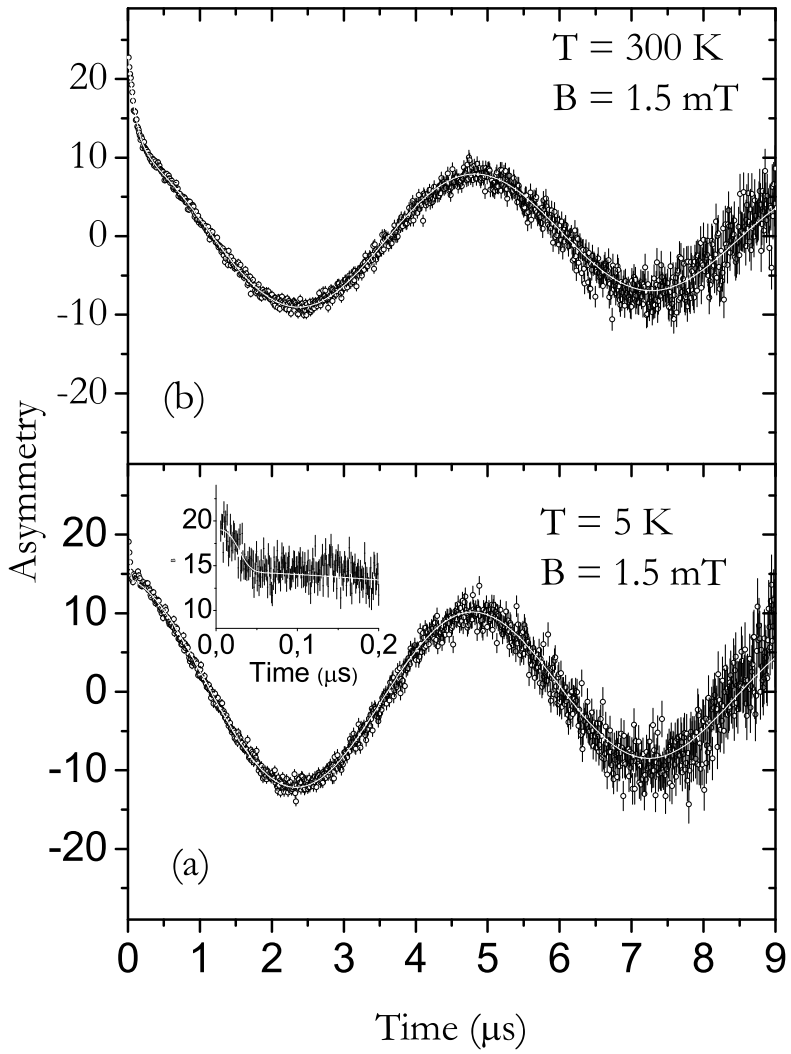

Figure 3.1: Muon spin asymmetry as a function of time, in transverse geometry (B =1.5 mT), at T =5 K (below), and at T =300 K (observed at PSI). A clear nearly undamped oscillation at the Larmor frequency is observed, which amounts to approximately 60% of the initial muon spin polarization at T = 5 K and to approximately 40% of the initial muon spin polarization at T = 300 K. A strongly relaxed signal is observed in the first few hundred nanoseconds. Lines are fits as discussed in the text.

We have undertaken very recently (June 2011) a transverse-field dependence study at room-temperature (at PSI). This study clarifies that the proper model for the data, at all fields, is that proposed in Eq.3.3. However, these data have not been analyzed to their full potential yet and therefore will not be included here. The essential conclusion remain unaffected.

The presence of these two relaxing components presents an experimental problem: on one hand, a clear definition of the slowly relaxing diamagnetic component benefits from the large time-window available only at ISIS; on the other hand, the pulsed nature of ISIS beam limits the observation of the highly relaxing component, which is best followed at PSI, with its quasi-continuous beam. A coherent overall picture can therefore be obtained only from a conjugation of the data obtained at both facilities.

It is visible that for the first tenths of a microsecond, the behavior is not identical (Fig. 3.1). That was confirmed while fitting the data, were we obtained two regimes: one for temperatures below 125K, and one above 125K. We will now discus both cases separately.

T <125 K

In this temperature spectrum tried to fit the fast relaxing component of equation 3.2 ($A_{\text{fast}}e^{-\lambda_{\text{fast}}t}$) with a Gaussian, Lorentzian, and compressed exponential $\exp(-(\lambda_{\text{fast}}t)^3)$. As we can see in Figures 3.2, and 3.3 the form of fast relaxation function fit that provides the best description is the compressed exponential.

As is illustrated in Fig.3.2, a lorentzian relaxation ($e^{-\lambda_{\text{fast}}t}$) does not provide a good fit to the fast relaxation observed at tow temperatures. Thus we have tried other options, such as a gaussian relaxation ($e^{-\sigma^2t^2}$) or a compressed exponential ($e^{-(\lambda t)^3}$); these are depicted in Fig.3.3 and clearly provide a better description (the compressed exponential being slightly better). We shall discuss the physical meaning of this below.

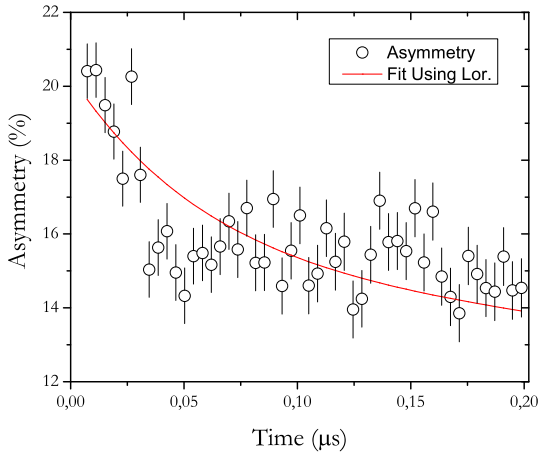

Figure 3.2: Muon spin asymmetry as a function of time (first 0.2μs), in transverse geometry (B =1.5 mT), at T =25 K (below), fitted with a lorenzian damped second component.

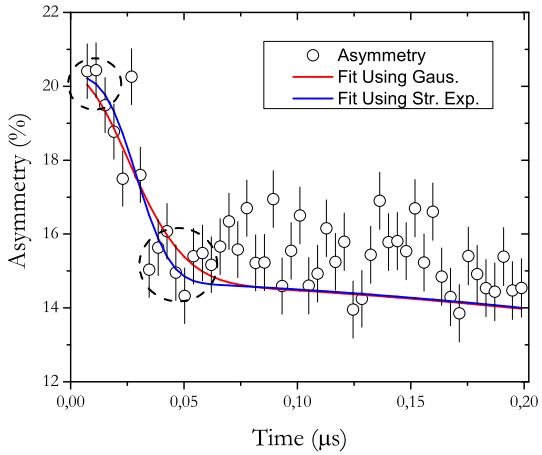

Figure 3.3: Muon spin asymmetry as a function of time (first 0.2μs), in transverse geometry (B =1.5 mT), at T =25 K (below), fitted with a gassian (red) and stretched exponential (blue) damped second component.

T >125 K

At these temperatures, a single Larmor precession signal with bi-exponential relaxation (Cf. Eq. 3.3) gives an adequate description of the data, as seen in Fig3.4. This means we have two distinct regimes affecting muon spin polarization as discussed below.

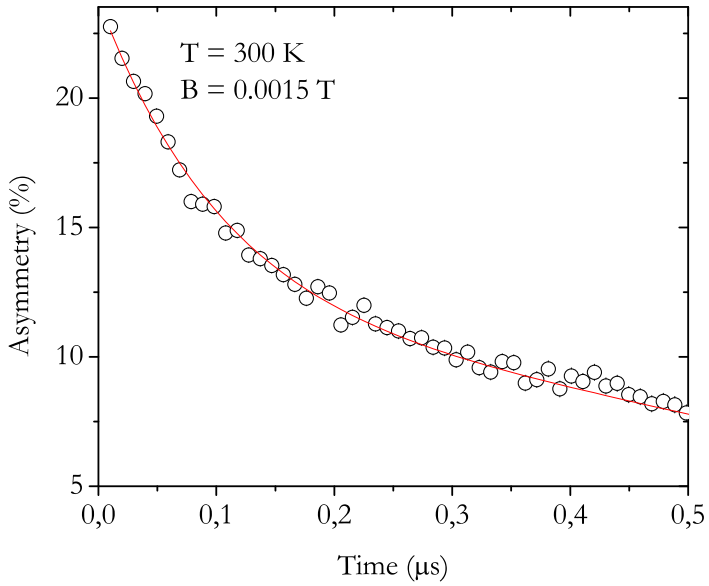

Figure 3.4: Muon spin asymmetry as a function of time (first 0.5μs), in transverse geometry (B =1.5 mT), at T =300 K (below), fitted with a lorenzian damped second component.

Overhall Results

Using the fits described above, we can obtain the data displayed in figures 3.5, 3.6, and 3.7.

In Fig.3.5 we display the fractions as a function of temperature between 5 and 300 K. These have been obtained by comparison of the fitted asymmetries A_{slow} and A_{fast} to the maximum instrumental asymmetry, as obtained from a calibration with silver.

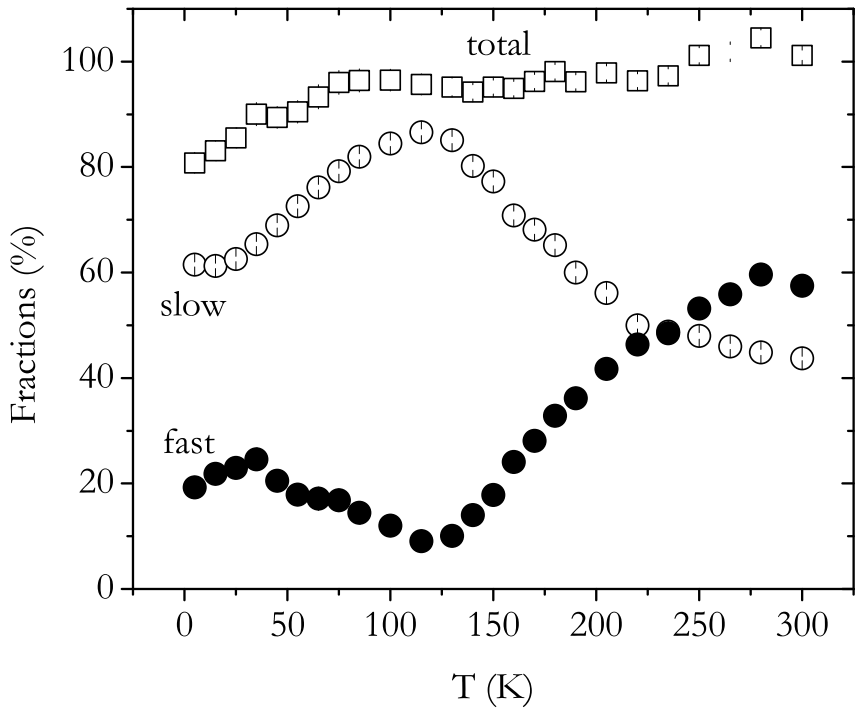

Figure 3.5: Temperature dependence of the slow diamagnetic component (open circles), the fast paramagnetic component (closed circles) and total fraction (open squares), as observed at PSI, for an applied transverse field B=1.5 mT.

In Fig.3.6 we display the relaxation rate $\lambda_{\rm slow}$ of the slowly relaxing fraction as function of temperature. The overall values are very low and could be measured only at ISIS with the long time window. A transverse field B = 2 mT was used. Two features are seen. At low temperatures a slightly enhanced relaxation is observed which decreases quickly with increasing temperatures.

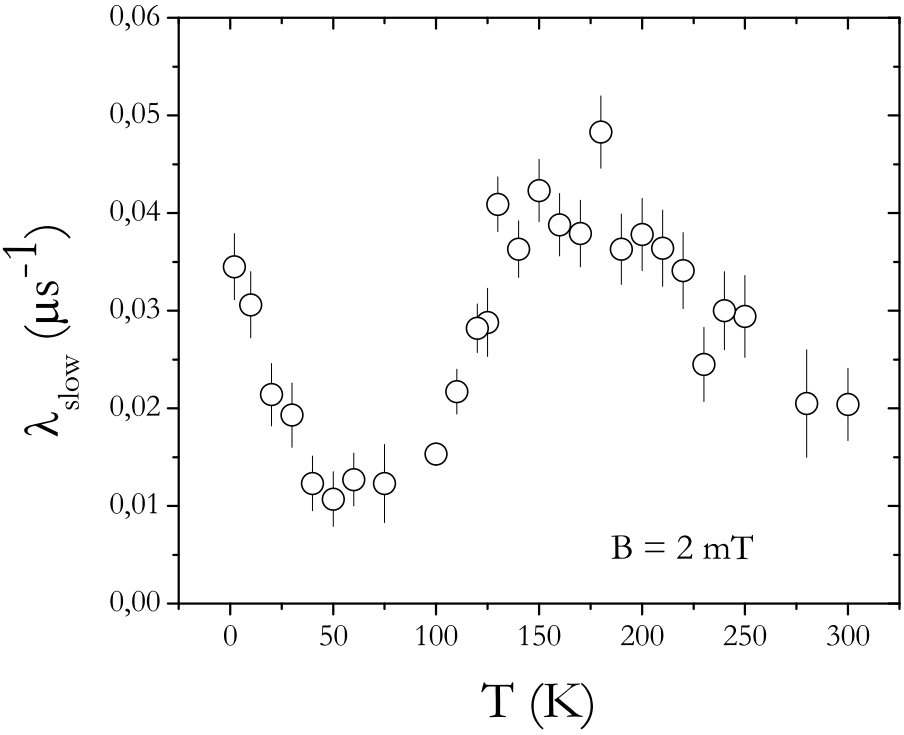

Figure 3.6: Temperature dependence of the slow Lorentzian relaxation λ_{slow}, observed at ISIS in transverse-field experiments (B=2 mT). The full line below 75 K is a fit to an activated process which we assign to the ionization of a shallow donor.

In Fig.3.7 we show that the relaxation rate λ_{fast} of the fast relaxing fraction as a function of temperature. Such a high relaxation can be caused only by a hyperfine interaction and thus indicates the presence of muonium, either directly formed as the muon stops in the sample or created later via charge state changes. The signal is defined by a few data points at the beginning of the time spectra only and therefore the extracted parameters depend on the actual relaxation function used, giving rise to systematic uncertainties not included in the error bars shown in the figure.

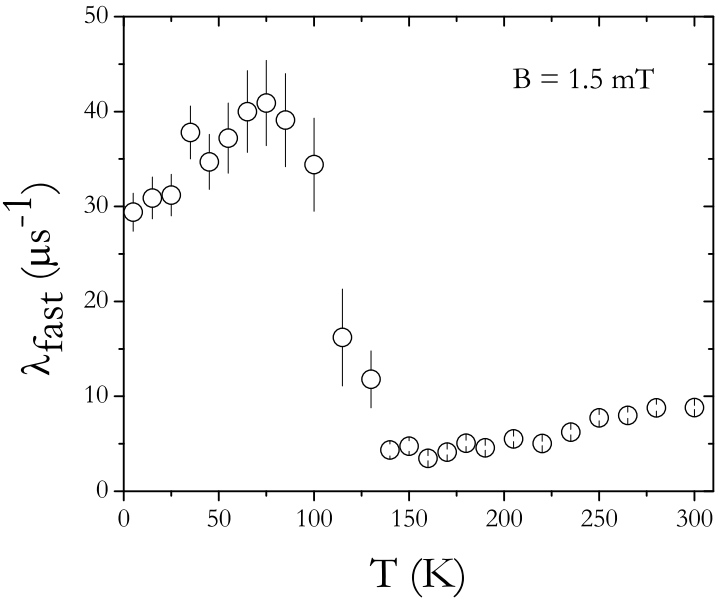

Figure 3.7: Temperature dependence of the paramagnetic relaxation λ_{fast}, observed at PSI in transverse-field experiments (B = 1.5 mT).

3.2.2 Longitudinal-Field Analysis

A typical spectrum is shown in Fig.3.8, for TeO_2 at room-temperature under a longitudinal-field of 2mT. Two relaxations are clearly visible, which arise from dynamical processes involving the muon spin.

We tried fitting this data using two components, like we did for the transverse-field:

$$A(t) = A_{\text{slow}} e^{-\lambda_{\text{slow}} t} + A_{\text{fast}} e^{-\lambda_{\text{fast}} t} \tag{3.4}$$

However we observed that for the low temperature régime (below 125 K) that was not possible, since only a slow relaxing component can be fitted; part of the muon polarization is missing. This is due to instrumental inability, at ISIS, to detect a signal with a very high relaxation rate, which can be seen in transverse-field at PSI Fig.3.7.

For the high temperature régime (above 125 K) that problem does not

arise (Fig.3.7) because the relaxation rate of the fast component is much smaller. These fits were then made with 2 components.

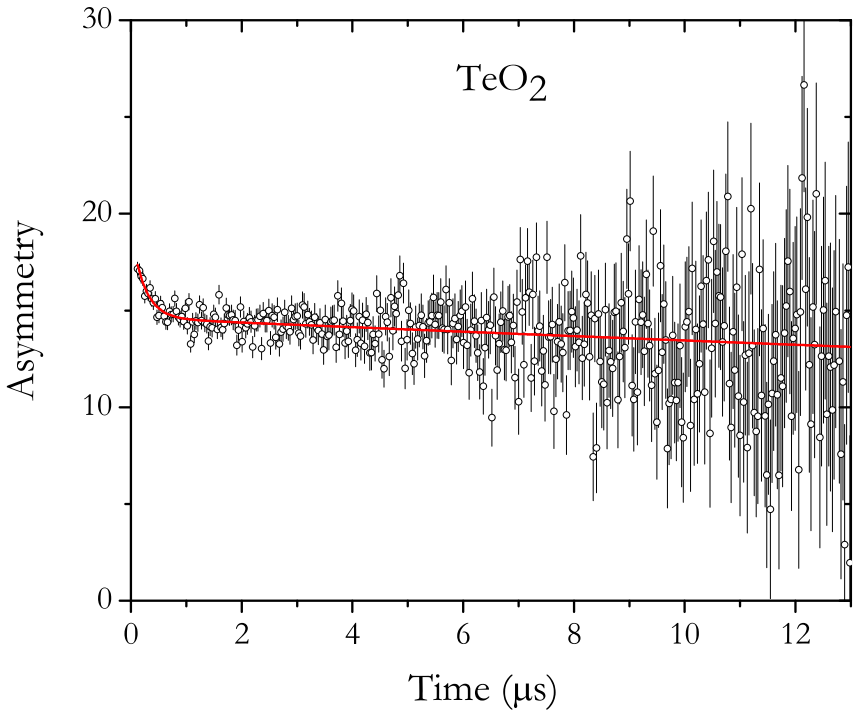

Figure 3.8: Time spectrum of a TeO_2 sample at T=300 K, subject to a longitudinal field of B=2 mT. The appearance of a relaxation in this nuclear-magnetic-moment-free compound is a sign of dynamical processes envolving the muonium states.

Using these fits we can obtain the data displayed in Fig.3.9, were we show that the recovery of the integral muon spin polarization as a function of the applied longitudinal magnetic field at 6 K. The main recovery occurs in the temperature range between about 50 and 500 mT indicating the decoupling of a muonium hyperfine interaction of about 3.5 GHz. The fraction was obtained from comparison to a silver calibration.

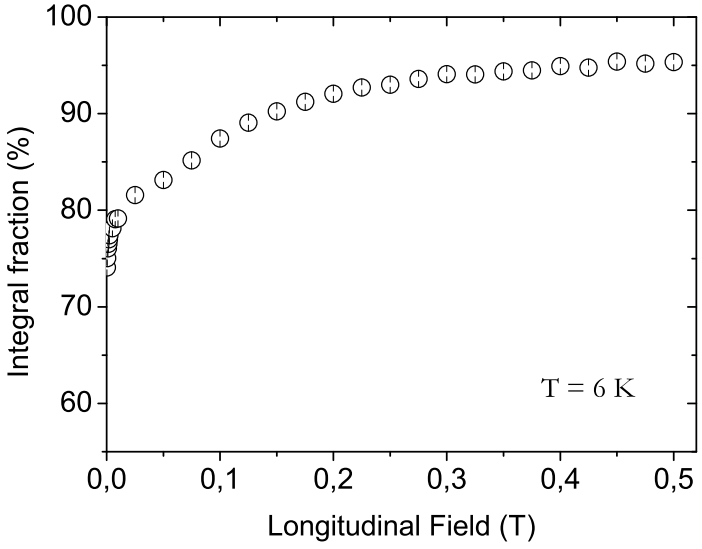

Figure 3.9: Dependence of the integral fraction with an applied longitudinal field, at T = 6 K, observed at ISIS.

3.2.3 Radio-frequency Analysis

The measurements were done at the HiFi instrument at ISIS, in a longitudinal-field of 2.3764T. An applied radio-frequency of 322MHz, corresponding to the resonant value for the muon spin in a diamagnetic environment, was applied to the sample volume, inducing a corresponding alternate- field, of a few tenths of mT, perpendicular to the main longitudinal-field.

Before starting the measurements a small longitudinal field scan is performed, using auxiliary coils, near the calibrated value for resonance, for tuning purposes. The optimized value for the field was 2.70(1) mT, as shown in Fig. 3.10.

A calibration using polyethene was performed. A temperature dependence study was done from 6K to 300K.

The resulting diamagnetic fraction in TeO_2 is shown in Fig.3.11.

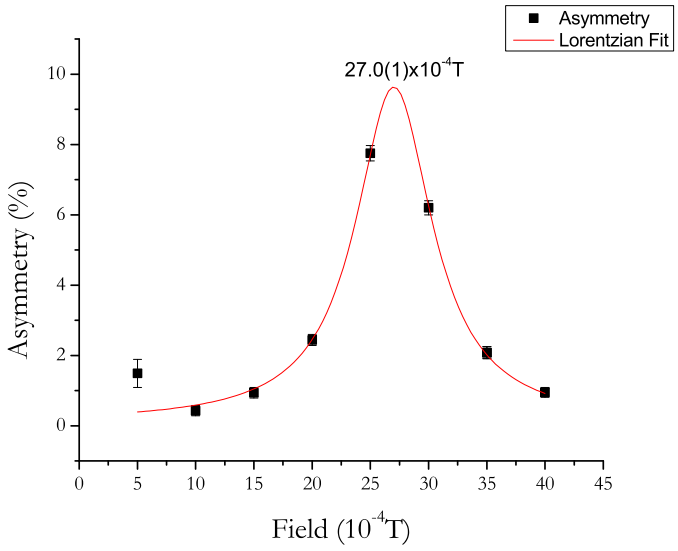

Figure 3.10: Radio-frequency field scan performed at 125K, in irder ti fine tune the resonant applied longitudinal-field.

After that measurements were made and analyzed as described in section 2.4.4 and the results are shown in Fig. 3.11.

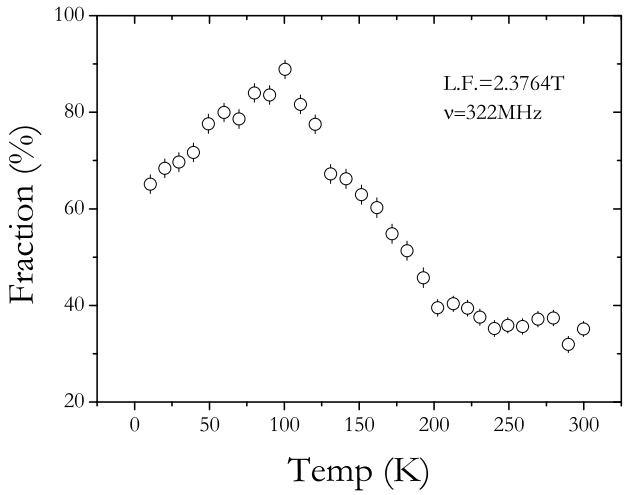

Figure 3.11: Temperature scan of the diamagnetic fraction in TeO_2, obtained using the radio-frequency setup at ISIS.

3.3 Interpretation and Discussion

In this section we will use the analyzed data from the previous section and interpret and discussing its physical meaning.

Below 125 K, the two signals appear to represent distinct diamagnetic and paramagnetic fractions. Thus in Fig. 3.1(a) we attribute the fast decay ($\lambda_{\text{fast}} > 30\ \mu\text{s}^{-1}$) to an overdamped precession signal of triplet-state muonium, promptly formed but very short lived. A oscillating 21 Mhz fit was tried, but because of the very fast relaxation only a quarter of an oscillation is visible, and therefore, the results of that fit are not satisfactory, however, we did observe, with those fits, that the period of oscillation of that overdamped precession signal is in fact of a 21 MHz nature. Because the compressed exponentials such as $\exp\left(-(\lambda_{\text{fast}}t)^3\right)$ is the fast relaxation function fit most similar to a quarter oscillation it provides the best description for the data in this temperature range. Another indication that this paramagnetic signal is in fact an overdamped precession signal of triplet-state muonium, promptly formed but very short lived is the fact that the missing and the fast-decaying fractions are equal, accounting in total for 40% of the incoming muons, seen in Fig.3.14.

3.3.1 Shallow-donor state and the donor level

We justify the decrease of λ_{slow} in Fig.3.12, obtained in with the transverse-field fits, with increasing temperature to the ionization of shallow-muonium. In this state the DFT calculations for TeO_2 [2] show that hydrogen (and therefore muonium) binds strongly to an oxygen ion of the lattice, forming a covalent bond; this configuration is normally denominated as the bond configuration (Fig.1.4). It could be argued that the decrease of relaxation could also be justified by diffusion of a particle in the presence of the magnetic field created by the nuclear magnetic moments (called motional narrowing) [58]. However, because the abundance of magnetic moments in TeO_2 is very low (the only significant natural isotope is ^{125}Te, with 7% abundance), and we may expect the corresponding Gaussian relaxation not to exceed $0.01\,\mu\text{s}^{-1}$, from calculations of the second moment of the magnetic field arising from

the nuclear moments [58] at the hydrogen sites determined from the ab-initio calculations [2], we can conclude that the origin of the observed relaxation is therefore electronic and not nuclear.

In principle, the formation of shallow muonium, i.e. of a bound hydrogenic state of an electron to the positive muon with an extremely small hyperfine interaction A (around few hundred kHz) will give rise to two additional frequency lines placed symmetrically around the diamagnetic line $\omega_\mu/2\pi$, at $\omega_\mu/2\pi \pm A/2$. However, if spin-flip dynamics exists or the instrumental resolution is not enough to resolve these lines, the effect will be that of a single broadened line at $\omega = \omega_\mu$ [1]. In the static case, the value of the broadening is of the order of magnitude of the hyperfine interaction, which points to a hyperfine interaction with an order of magnitude about 10 kHz, which compares with similar values for other oxides [1]. The decrease of this broadening with increasing temperature thus corresponds to the ionization of the bound shallow muonium state in the donor-like process.

$$\mathrm{Mu}_\mathrm{D}^0 \rightarrow \mathrm{Mu}_\mathrm{D}^+ + e_\mathrm{CB}^- \tag{3.5}$$

In order to fit the decrease in λ_{slow}, we took the weighted average of the relaxation λ_+, of the muons in the pure diamagnetic state, and of the relaxation λ_0, of the muons in the shallow paramagnetic state,

$$\lambda_d = f_0\lambda_0 + f_+\lambda_+ \tag{3.6}$$

where the formation probability f_0 of the shallow paramagnetic state is assumed to have the phenomenological Boltzmann dependence [1]

$$f_0(T) = \frac{1}{1 + N\exp(-E_a/k_\mathrm{B}T)} \tag{3.7}$$

where E_a is the activation energy of the process, k_B is the Boltzmann constant and the empirical parameter N relates to the density-of-states. The normalized formation probability of the corresponding diamagnetic state obeys $f_+ = 1 - f_0$. These formation probabilities are normalized to the total diamagnetic fraction f_d observed at low temperatures. One obtains (for a fixed

λ_0) the proportionality between the relaxation rate λ_d and the paramagnetic fraction f_0 for $\lambda_+ = 0$. In the fit shown in Fig.3.12, the relaxation of the diamagnetic state was fixed to $\lambda_+ = 0.01\ \mu s^{-1}$, and an activation energy $E_a = 6(2)$ meV (with $N = 3(2) \times 10$, $\lambda_0 = 0.033(2)$ MHz).

From this value, and using $\epsilon = 24(1)\epsilon_0$ [38, 39] for the static dielectric constant in $\alpha-TeO_2$, we may estimate [1] the electron effective mass to be $m^* = 0.3(1)m_0$ and the hyperfine interaction to be around 0.05 MHz (corresponding to a Bohr radius of about 50 Å).

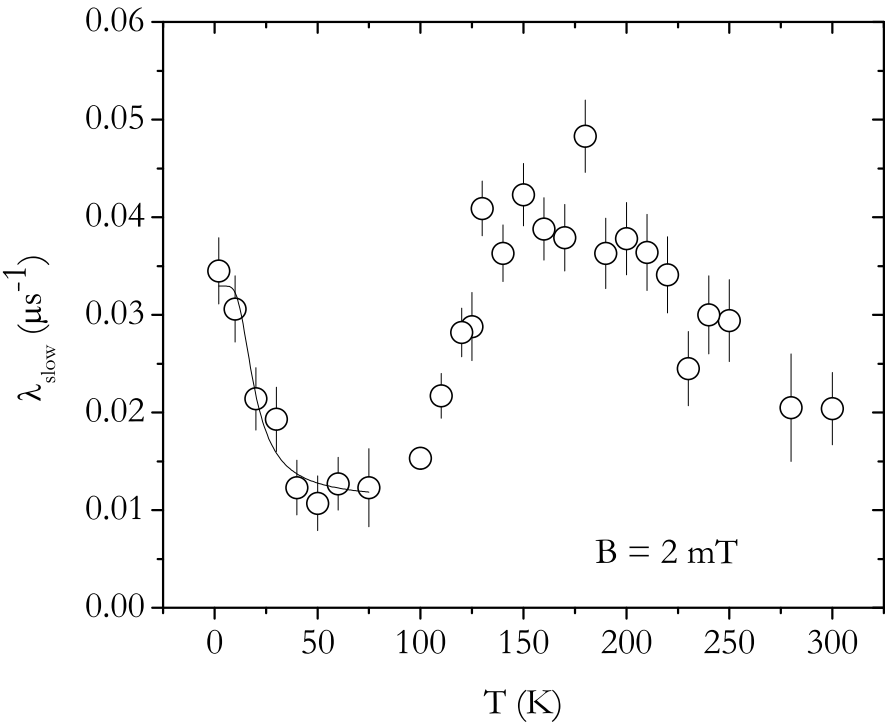

Figure 3.12: Temperature dependence of the slow Lorentzian relaxation (λ_{slow}) with fit, observed at ISIS in transverse-field experiments (B = 2 mT).

3.3.2 Atom-like (deep) muonium

A repolarization curve is seen (Fig.3.13) in longitudinal-field experiments, performed at T = 6 K, corresponding to a hyperfine interaction of about 3.5

GHz. The interaction is isotropic or almost isotropic and its value amounts to about 78% of the vacuum value, if we exclude fields lower than 250mT (the inclusion of that part will be explained in the next chapter of this dissertation); this exclusion does not however influence the essential as aspects of the analysis below.. This is the signature of an atom-like state with little interaction with the surroundings. It is usually assumed that this so-called deep or normal muonium resides at an open interstitial site in the lattice [59]. In Ref. [2] we see that the DFT calculations determined a higher-energy metastable configuration of neutral hydrogen with the latter residing deeper in the interior of the ring structure of the lattice.

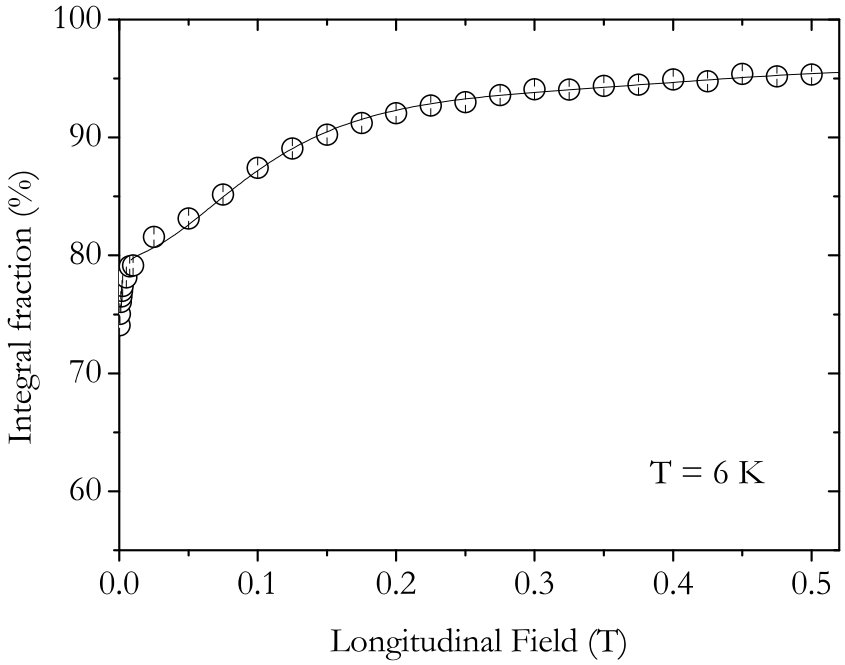

Figure 3.13: Dependence of the muon spin polarization with the applied longitudinal magnetic field B, for TeO_2 at T=6 K an isotropic muonium state with $A = 3.5(1)$GHz. The spin polarization is shown to vary from 73% at zero-field up to 96% at high-fields.

In low transverse field, the singlet-triplet transition frequency of ca. 3.5

GHz is far too high to be resolved (Fig.2.2), as is the case in study, so that half the polarization is lost. As we discussed above, the other half would normally be seen as an intra-triplet precession signal, with frequency 21 MHz at 1.5 mT. but in the case of TeO_2 it appears to be damped in less than one cycle, mainly reflecting the short lifetime of the quasi-atomic state, we is much to fast of a decay to be detected in ISIS facility. The equality of the missing and fast-decaying fractions support this interpretation, accounting in total for 40% of the incoming muons.

3.3.3 Conversion dynamics

We can see in Fig.3.14 that at low temperatures, about 60% of the muons form the donor configuration and about 40% form the atom-like muonium, as discussed above. However, this ratio is temperature dependent as evidenced by the increase and decrease of the slowly relaxing component, with a maximum at about 125 K. The increase can be assigned to a conversion of paramagnetic deep muonium to diamagnetic muonium (which can correspond to Mu^+ or Mu^-, not specifying the charge state at this stage). Consequently, we can assign the decrease to a reverse reaction, $Mu^{+,-}$ converting to Mu^0. In this last case, charge fluctuations seem to play a non-negligible role. In the following subsections we concentrate the discussion on the fractions represented in Fig.3.14, obtained as described in the previous section, from which an activation energy for the ongoing processes can be extracted. We refrain, in this chapter, from the corresponding analysis of the relaxations shown in Fig.3.12 and 3.15, the clarification of such processes requires an extensive research program built upon the results of the current work, in order to clarify the specific processes involved and build and adequate model such as the one currently existing for intrinsic silicon [15]. Such a model should also include indirect interaction with defects and impurities. However, the temperature dependence of the fractions contains already the basic feature relative to the conversion of the muonium states present.

Conversion of Mu^0 to $Mu^{+,-}$ (T < 125K)

Experimentally we can not distinguish between Mu^+ and Mu^- and therefore no definite assignment can be made to the final state being formed.

If we assume, as before, a phenomenological Boltzmann partition between the two configurations

$$f_{\text{fast}}(T) = \frac{1}{2}\frac{f_p}{1 + N_1 \exp(-E_1/k_{\text{B}}T)} \tag{3.8}$$

$$f_{\text{slow}}(T) = \frac{f_p N_1 \exp(-E_1/kT)}{1 + N_1 \exp(-E_1/k_{\text{B}}T)} + f_d \tag{3.9}$$

where f_d and f_p are the total formation probabilities of the diamagnetic and atom-like paramagnetic configurations, respectively, and $f_d + f_p = 1$ or $f_p = 1 - f_d$. E_1 is the activation energy of the process, k_B is the Boltzmann constant and the empirical parameter N_1 relates to the density of states. Note that the index 1 is used here to distinguish the parameters used in Eq. 3.6 and Eq.3.7 from those used for the processes described in the next paragraph, where we use index 2. The factor 1/2 in the Eq.3.7 accounts for the fact that only half of the Mu^0 frequencies are visible for deep muonium, as described in subsection 3.3.2, the other half of the transitions being not detected due to their high frequencies. The simultaneous fit of Eq.3.7 and Eq.3.8 to the data below T = 125 K is represented in Fig.3.14 (full lines), yielding $f_d = 61.6(5)\%$, $N_1 = 6(1)$ and an activation energy $E_1 = 13(1)$ meV.

Possible assignments for these transitions are:

The Mu^0 to Mu^+ conversion, where the site change of interstitial muonium to the bond donor configuration, accompanied by a loss of the electron. In this case the activation energy (E = 13 meV) extracted from the increase of the slowly relaxing fraction would represent the barrier height for the conversion. This process would then correspond to a deep to shallow conversion of the neutral state, with simultaneous ionization above 50 K.

The Mu^0 to Mu^- conversion, which is the process also proposed for the ZnSe case [9, 60], and which the current DFT calculations depict it as very probable here as well, since the existence of a stable negatively-charged hy-

drogen state in the deep interstitial geometry is predicted [2]. This interpretation assumes that in these heavily compensated materials radiolytically produced conduction electrons are temporarily stored at the native donors and liberated at the temperature where ionization occurs. These electrons can then be captured at interstitial muonium to form Mu^-. In this case the 13 meV activation energy extracted from the fit in Fig.3.14 below 125 K represents the ionization energy of the native donors.

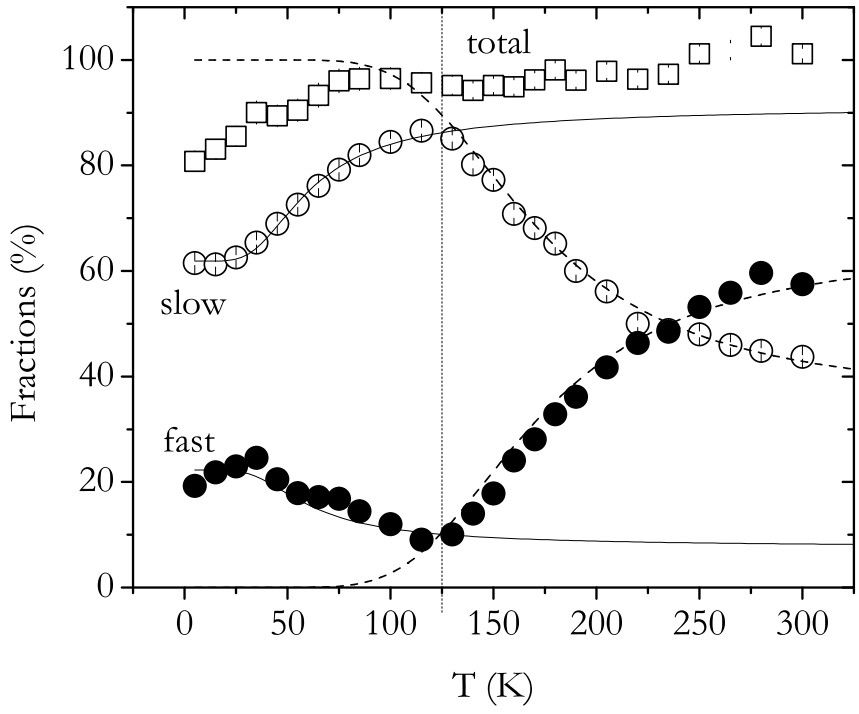

Figure 3.14: Temperature dependence of the slow component (open circles), the fast component (solid circles) and total fraction (open squares) with fit, as observed at PSI, for an applied transverse field (B = 1.5 mT).

The fist case scenario seems a very plausible explanation and is consistent as well with the DFT-NEB calculations for hydrogen [2], where a very low barrier is obtained. However, a problem arises for the temperatures above 125 K where apparently the reverse reaction occurs. The bond donor con-

figuration is a very stable situation and a re-formation of the higher-energy interstitial state seems unlikely: it would require the breaking of a strong covalent bond with oxygen. The DFT-NEB calculations [2] for the barrier of the path leading to such a re-formation provide a magnitude of 1.4 eV, suggesting this to be a very difficult process.

Conversion of $Mu^{+,-}$ to Mu^0 (T > 125 K)

Above 125 K, the slowly relaxing diamagnetic muonium fraction decreases (Fig.3.14) meaning that the configuration becomes unstable. We can assume that a deep muonium state is formed, at least temporarily, because of the high relaxation value of the fast relaxing component (Fig.3.15). This reverse process can explain the decay of the slowly relaxing component in Fig.3.14 and it is possible to extract an activation energy by fitting the fractions with Boltzmann distributions analogous to the model described in Eq.3.7 and Eq.3.8 (where the factor 2 in Eq.3.7 is now removed to take into account that the entire muon polarization is now observed). The resulting simultaneous fit to the two fractions for T > 125 K is represented in Fig.3.14 and yields $f_d = 33(3)\%$, $N_2 = 66(30)$ and an activation energy of 63(5) meV.

In case the possible processes are the inverse conversions discussed in the previous subsection and correspond to:

The Mu^+ to Mu^0 conversion, in which the re-activation of muonium from the bond site to the interstitial site, this value would represent the energy difference of the neutral muonium in the two configurations, respectively. 63 meV seems too low for this level difference, compared to 1.4 eV predicted by DFT [2].

The Mu^- to Mu^0 conversion, were the loss of the second electron in Mu^- may easily be lost either to the valence band filling holes if present [61] or to the conduction band [9]. However, 63 meV seems too low for the later case, since the theoretical DFT predictions place the thermodynamic $\epsilon(0/-)$ level about midgap, and the $\epsilon(0/-)$ level associated to the interstitial hydrogen configuration even lower (see Fig.1.2). In the former case (hole capture), the activation energy corresponds to the activation energy of the native acceptors

and 63 meV appears as a most sensible value.

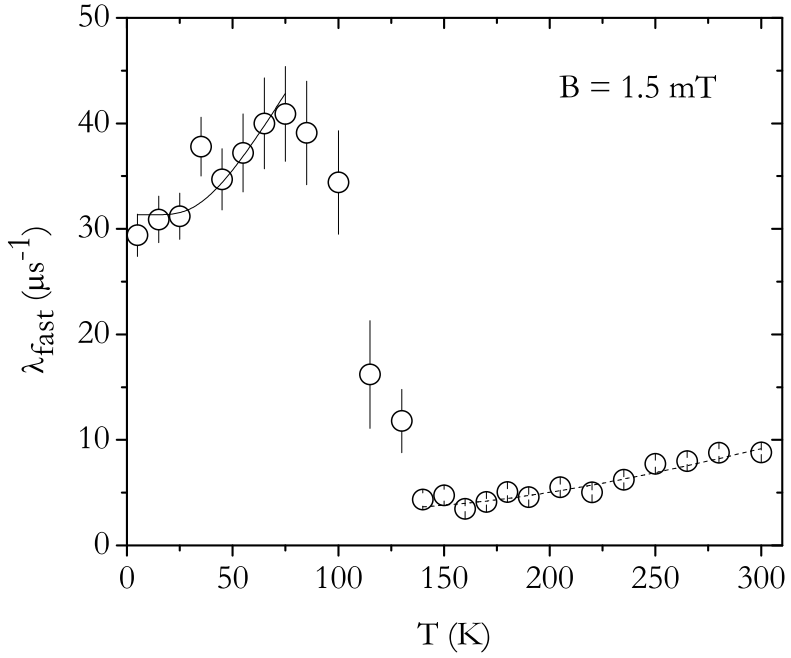

Figure 3.15: Temperature dependence of the paramagnetic relaxation (λ_{fast}) with fit, observed at PSI in transverse-field experiments (B = 1.5 mT).

Corroborating Radio-Frequency Data

The diamagnetic evolution is corroborated by the radio-frequency data represented in Fig.3.16 along with the transverse-field data of Fig.3.14. We can se that for the low temperature regime (T < 125 K) the diamagnetic and radio-frequency fractions coincide in value and evolution. On the other side for the high temperatures (T > 125 K) we observe that only the evolution coincides, and that there appears to be a shift of the values. That can be explained by a relaxation of the radio-frequency reference signal, Fig.3.17 (signal that is measured the radio-frequency off), which originates underestimation of the fraction. The motive of this relaxation will be discussed in the next chapter of this thesis.

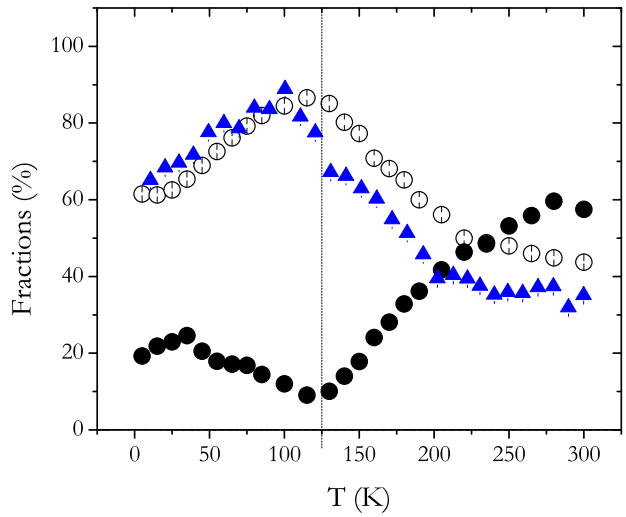

Figure 3.16: Temperature dependence of the slow component (open circles), the fast component (solid circles) and radio-frequency component (triangles squares), as observed at PSI (Transverse-Field) and ISIS-HiFi (Radio-Frequency).

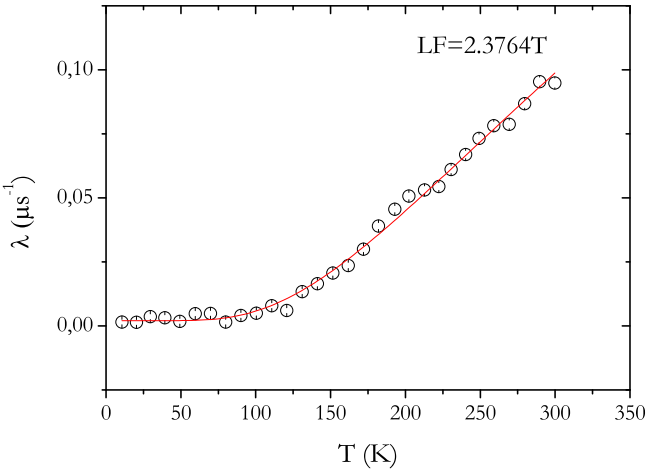

Figure 3.17: Temperature dependence of the relaxation of the radio-frequency reference signal with an applied longitudinal field of 2.3764T, ISIS-HiFi.

Chapter 4

Conclusions and perspectives

4.1 Towards a final synthess

We will now summarize the essential conclusions of the experimental data analysis and discussion made in chapter 3, which, as discussed in chapter 1, allow to conclude about the hydrogen configurations in α-TeO_2 due to the muonum/hydrogen analogy.

4.1.1 Summary

In this work we observed a donor and the higher-energy interstitial configurations both confirmed by a theoretical DFT calculations [2]. However, unlike in those calculations we have no experimental indication of the formation of the acceptor-like configuration where the muonium is strongly bound to the lattice. We suppose that the formation of this configuration is hindered by the requirement of the strong geometrical rearrangements to form it.

The donor configuration is experimentally observed mainly as ionized muonium (Mu^+) none the less a faint indication of a hyperfine interaction remains indicating that a weakly bound electron is present. The $\epsilon(+/0)$ conversion level can be located near the conduction band edge within a range of about ~ 6 meV, studying the disappearance of this interaction with temperature. This result is consistent with the theoretical DFT prediction [2].

The deep interstitial configuration is evidenced by the observation of atomic-like deep muonium with a hyperfine interaction of about 3.5 GHz, corresponding to about 78% of the vacuum value. The two other neutral muonium configurations would not show this characteristic. The formation Mu^- attributed to electron capture by the interstitial muonium can explain the gradual increase of the diamagnetic faction with temperature up to 125 K observed experimentally, the decrease of this fraction above 125 K is consequently due to the loss of the second electron forming Mu^0 again. However, as discussed above this interpretation is not unique model, however it is the model that raises fewer problems.

4.1.2 Hydrogen Configurations

We may now revisit the discussion done in Chapter 1, about the hydrogen configurations in TeO_2 and conclude that in α-TeO_2 hydrogen has also a a donor and the higher-energy interstitial configurations confirmed by these experimental results. We now have a clear picture of the donor and acceptor configurations (Figs.1.2, 1.4 and 1.3). We do not observe however the most stable acceptor-like configuration, which corresponds to an extended defect unobservable by μSR (Cf. Fig.1.2). In conclusion by combining experimental and DFT study [2] we obtain a quite complete picture of the basic behavior of isolated interstitial hydrogen in α-TeO_2.

4.2 Future developments

4.2.1 Open questions

Acceptor ionization

The dynamics of the acceptor state was not fully clarified. In order to address this question, transverse-Field data from PSI were taken in June of this year, which were not fully analyzed yet. However, a preliminary analysis shows no significant variation in the fractions from 300K to 600K. Above 600K a big variation is observed, but it is most likely due to the diffusion of

oxygen, which alters the chemistry of the sample.

Interaction with charge-carriers

Hall effect studies were attempted to study the conductivity type of the α-TeO_2 sample, however due to the oxygen diffusion mentioned above it was not possible to obtain ohmic contacts with the techniques we used. New techniques are being studied and will be attempted in a near future.

Details of the dynamics under 125K

As mentioned above, below 125K there is a conversion from a diamagnetic state to a paramagnetic state, most likely formation of Mu^-. However, in order to obtain a more detailed vision on the formation of Mu^-, we analyzed the sample at different temperatures using the longitudinal-field technique. In addition to that, there still is the question of the low field points which can not be fitted simply by using a simple isotropic state.

We will begin by addressing the latter case in which two indistinguishable solutions can be possible. In both outcomes a two state model is implied. In one case we have a model with two isotropic states: one atomic and one radical (with a slight change in its hyperfine constant). In the other we have two atomic states, in which one is slightly anisotropic. This remains an ongoing debate: Fig. 4.1 shows fits made in Quantum [62] using both models, which are indistinguishable.

Longitudinal-field data at 50K and 100K reveal that an isotropic stat model looks apparently good (Fig. 4.2 and Fig.4.3), though it implies hyperfine interactions that are not physically acceptable (5.8(2) GHz and 10.9(9) GHz). This is a clear sign of the ongoing muonium dynamics, which was not fully modeled up to now.

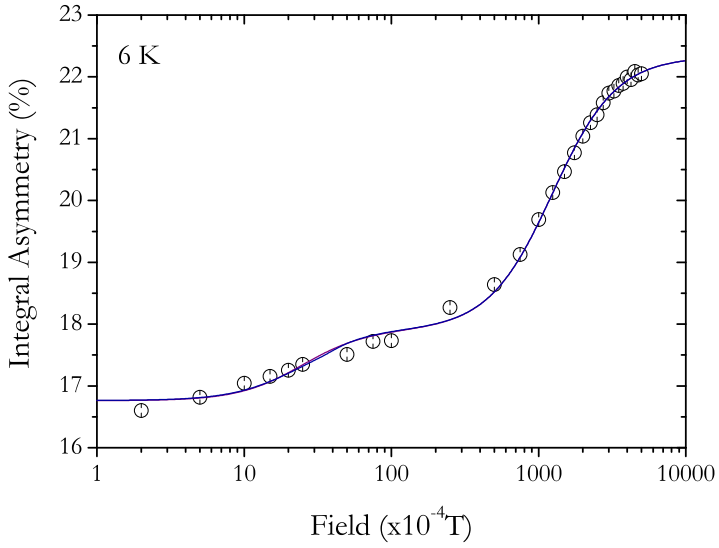

Figure 4.1: Data of Fig. 3.13 using the model described in the paragraph above.

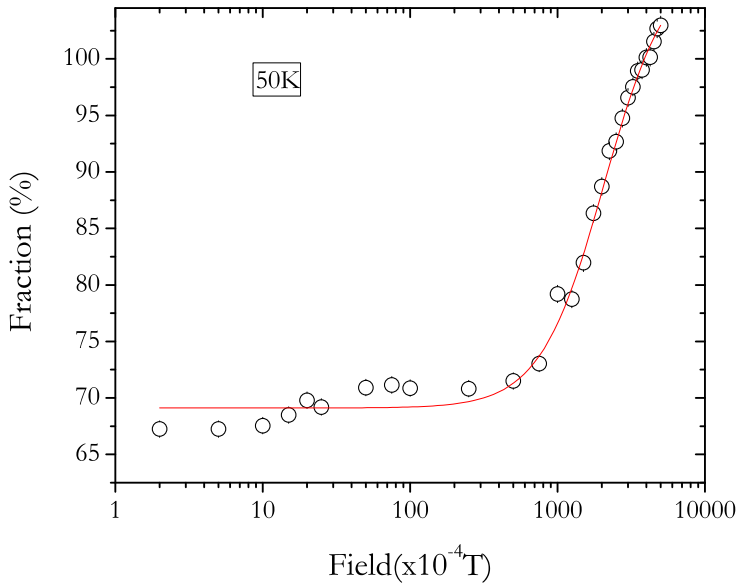

Figure 4.2: Repolarization curve obtained at ISIS at 50K, fitted assuming one atomic isotropic state.

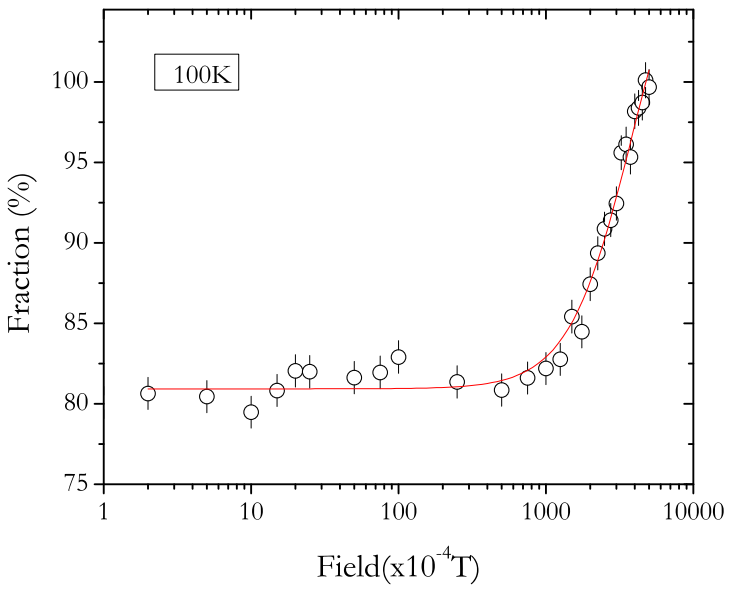

Figure 4.3: Repolarization curve obtained at ISIS at 100K, fitted assuming one atomic isotropic state.

A preliminary attempt to modeling these data was done using the Invanter and Smilga dynamical model [63] (Fig. 4.4 and 4.5). The fits are however very crude (also when using the Nosov-Yakovleva model [64]), implying a dedicated model needs to de developed.

A fit with two components (Fig.4.6) was also tried for the 50K data was one using two components, since a remarkable amount of dynamical situations seem o present bi-exponential relaxation in longitudinal-field [65]. A fit to the total asymmetry using a simple isotropic model gives good results, even fixing the same hyperfine constant obtained from the transverse-field data (Chapter 3). Note that these two components do not correspond to those observed in transverse-field, as explained for the 6K data; and the physical meaning of these two components are at this moment still in discussion.

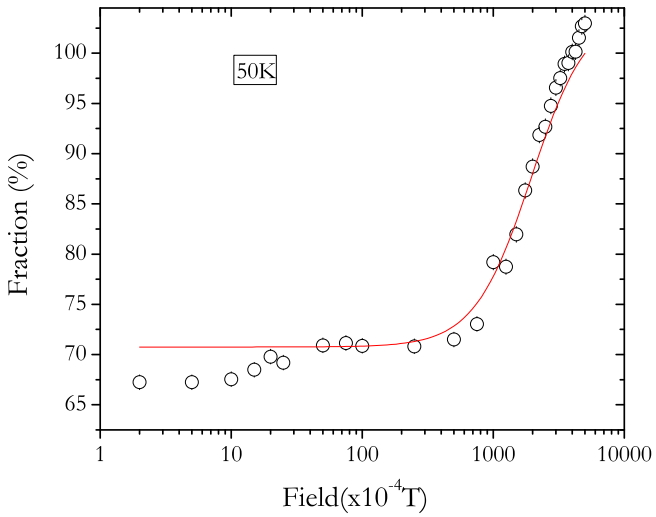

Figure 4.4: Repolarization curve obtained at ISIS at 50K, fitted assuming the Ivanter and Smilga approach.

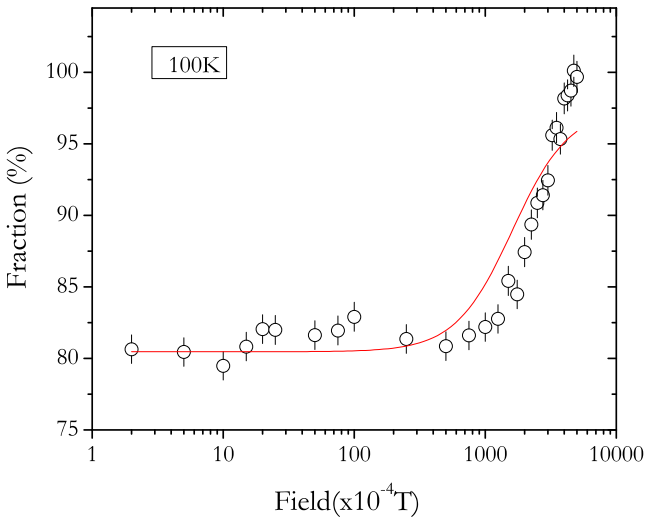

Figure 4.5: Repolarization curve obtained at ISIS at 100K, fitted assuming the Ivanter and Smilga approach.

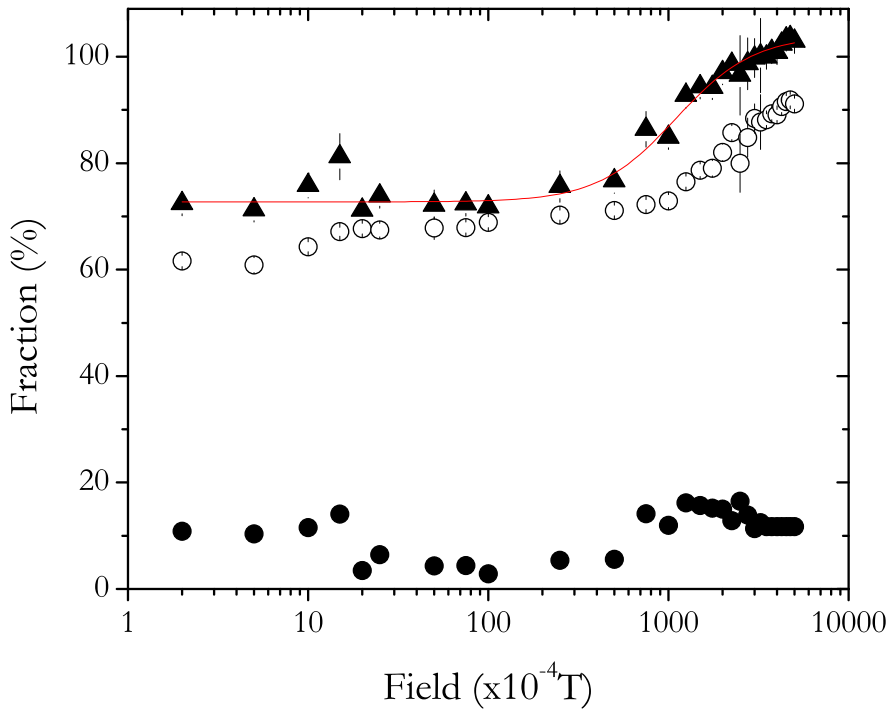

Figure 4.6: Repolarization curve obtained at ISIS at 50K, fitted using two components, one with a lorentzian relaxation and one with out.

Details of the dynamics over 125K

For the dynamics above 125K we propose a model which implies that the formed Mu^- ionizes with a fast rate forming Mu^0, which may recapture an electron, at a slower rate, forming again Mu^-.

We simulated this model using Quantum [62] maintaining a 40% non interacting Mu^+ and a 60% converting Mu^-, as described above. We used a fast ionization rate of 10 GHz and a slow capture rate of 10 MHz, obtaining Fig.4.7, which has a behavior very similar to that of the transverse-field raw data for 300K (Fig.4.8). After that we tried a preliminary fit, using this model, to the data and obtained relaxation rates of 500 $\pm$ 1800 MHz for the ionization rate, and 10 $\pm$ 4 MHz for the capture rate, Fig.4.8.

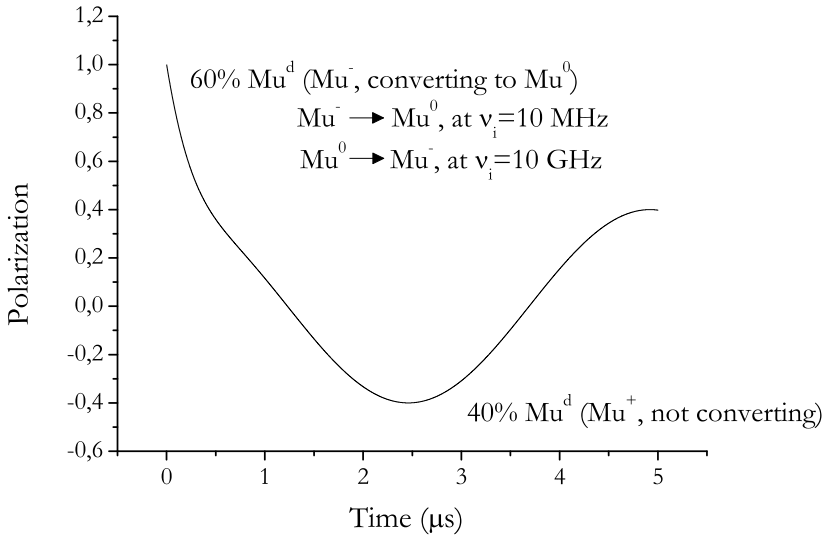

Figure 4.7: Simulation made in Quantum program, described in paragraph above.

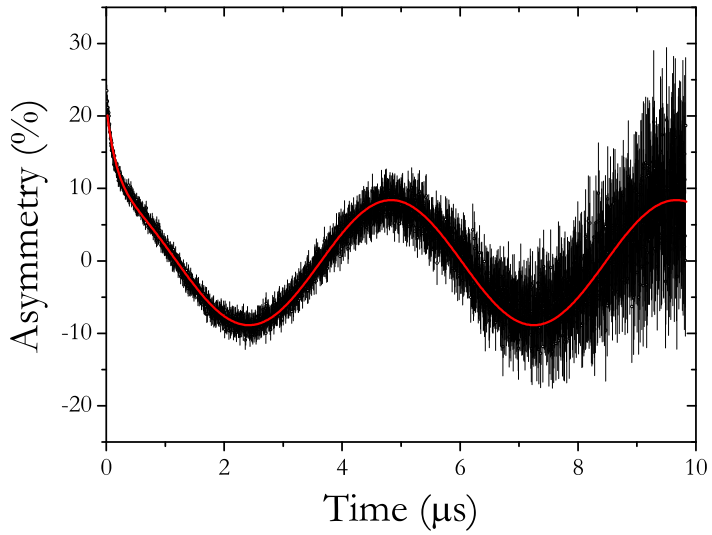

Figure 4.8: Fit made in Quantum program, described in paragraph above, to transverse-field raw data for 300K obtained in PSI.

Another way to test the model, and that will be done in the near future, is to fit the repolarization curve at 300K (Fig.4.9). In this case the raw data were fitted using two relaxed components, which in this case correspond in principle to the fractions obtained from the transverse-field data (Fig. 3.14), because the fast relaxation rate is now observable at the ISIS instrument. Here, because of the stability of the fractions until nearly 1T , we can assume that the dynamical process is very strong.

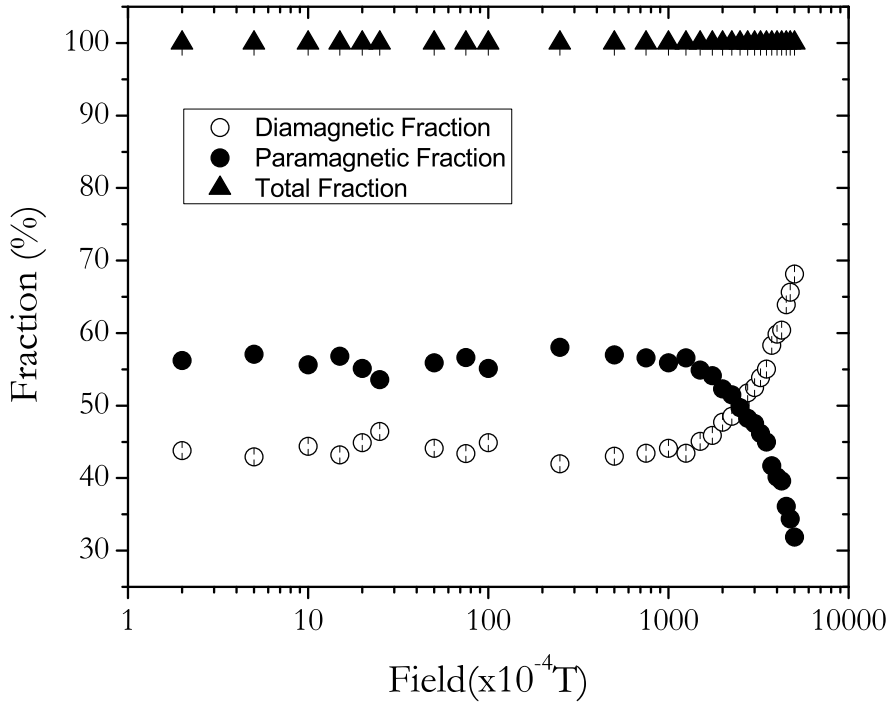

Figure 4.9: Repolarization curve obtained at ISIS at 300K, fitted using two relaxing components.

Attempts to obtain information concerning this temperature span using the transverse-field slow relaxation temperature scan were made, using Kim Chow's model [17] (Fig. 4.10). But this was not successful because the conversion rates were unphysical. So we concluded that the presuppositions of this dynamical model are not valid for this case.

A full model of the data, including the description of the field-dependance of the relaxation is currently being addressed.

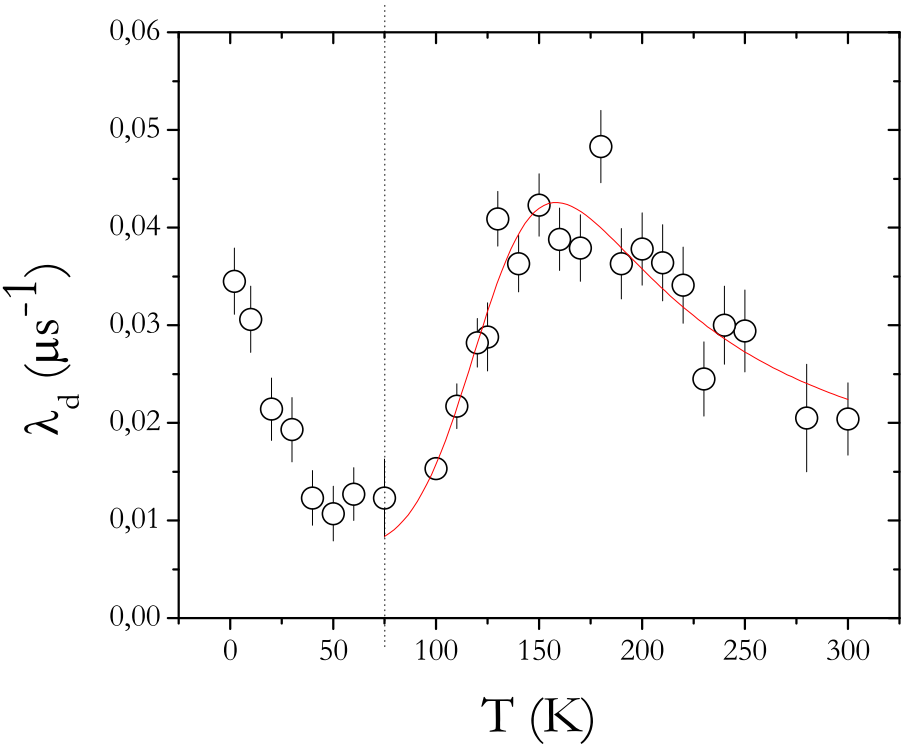

Figure 4.10: Transverse-field slow relaxation temperature scan, obtained at ISIS, fitted using Kim Chow's model.

4.2.2 Related investigations

We have begun to address the problem of isolated hydrogen in other relevant oxides, in particular yttrium oxide (Y_2O_3). Basic transverse-field data were acquired at PSI, at T.F.=15mT, from 6K to 300K. In this case a three component fit is needed to obtain a good fit to the transverse-field data (Eq.4.1). The muonium line at 21MHz is clearly visible, unlike in the case of TeO_2. We have thus fitted the asymmetry data to:

$$A(t) = A_{\mathrm{diamag}} e^{-\lambda_{\mathrm{diamag}} t} cos(\omega t + \phi_{diamag}) + A_{\mathrm{Mu}} e^{-\lambda_{\mathrm{Mu}} t} cos(\omega t + \phi_{Mu}) + A_{\mathrm{fast}} e^{-\lambda_{\mathrm{fast}} t} \tag{4.1}$$

Figures 4.11, 4.12, 4.13, and 4.14 represent temperature dependence of the fractions (upon comparison to the silver calibration), the diamagnetic, muonium, and fast relaxations, respectively. Fig.4.15 and Fig.4.16 are the result of DFT calculations, done in ongoing parallel theoretical work by Dr. Apostolos Marinopoulos and Estelina Silva Ref. [4]. These figures reveal already the basic behavior of hydrogen in Y_2O_3. We can associate the diamagnetic signal to a shallow donor like muonium, as in Ref. [1], and the paramagnetic signal to an acceptor like deep muonium configuration. The fast signal is not easy to interpret, though its fast relaxation clearly indicates an association with muonium. It could correspond to an unstable deep-acceptor configuration which is converting to another more stable configuration, either the other deep muonium or the shallow muonium, or, though that seems more farfetched, it could correspond to some of the previous two configurations which is being formed by an alternative (much slower and more spin-depolarizing) route, as in Ref. [28].

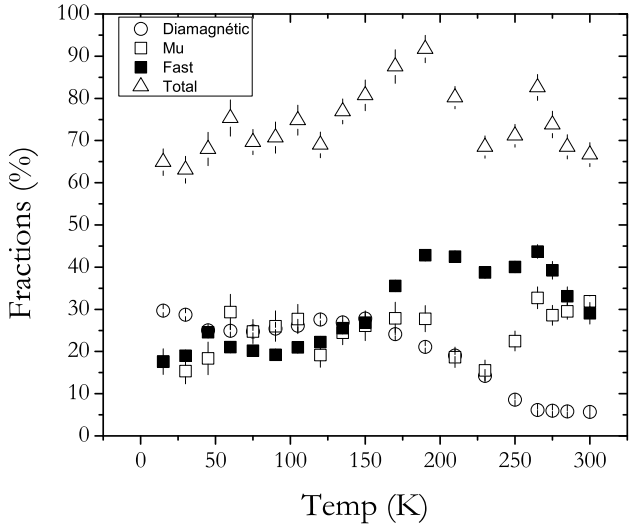

Figure 4.11: Temperature dependence of the diamagnetic component (open circles), the muonium component (open squares), the fast component (solid squares) and total fraction (open triangles), as observed at PSI, for an applied transverse field (B = 1.5 mT).

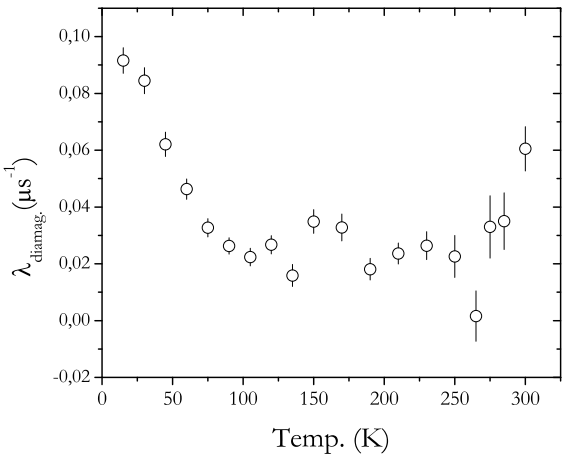

Figure 4.12: Temperature dependence of the diamagnetic relaxation component, as observed at PSI, for an applied transverse field (B = 1.5 mT).

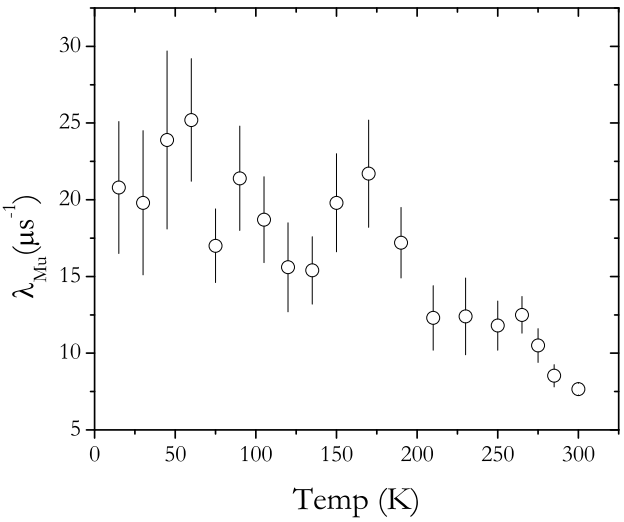

Figure 4.13: Temperature dependence of the muonium relaxation component, as observed at PSI, for an applied transverse field (B = 1.5 mT).

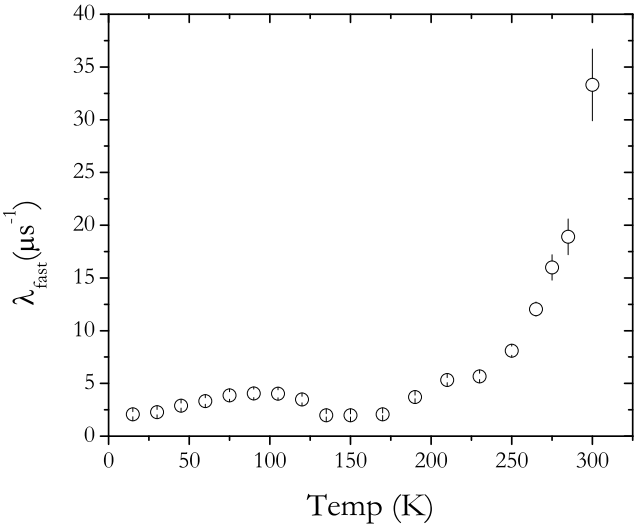

Figure 4.14: Temperature dependence of the fast relaxation component, as observed at PSI, for an applied transverse field (B = 1.5 mT).

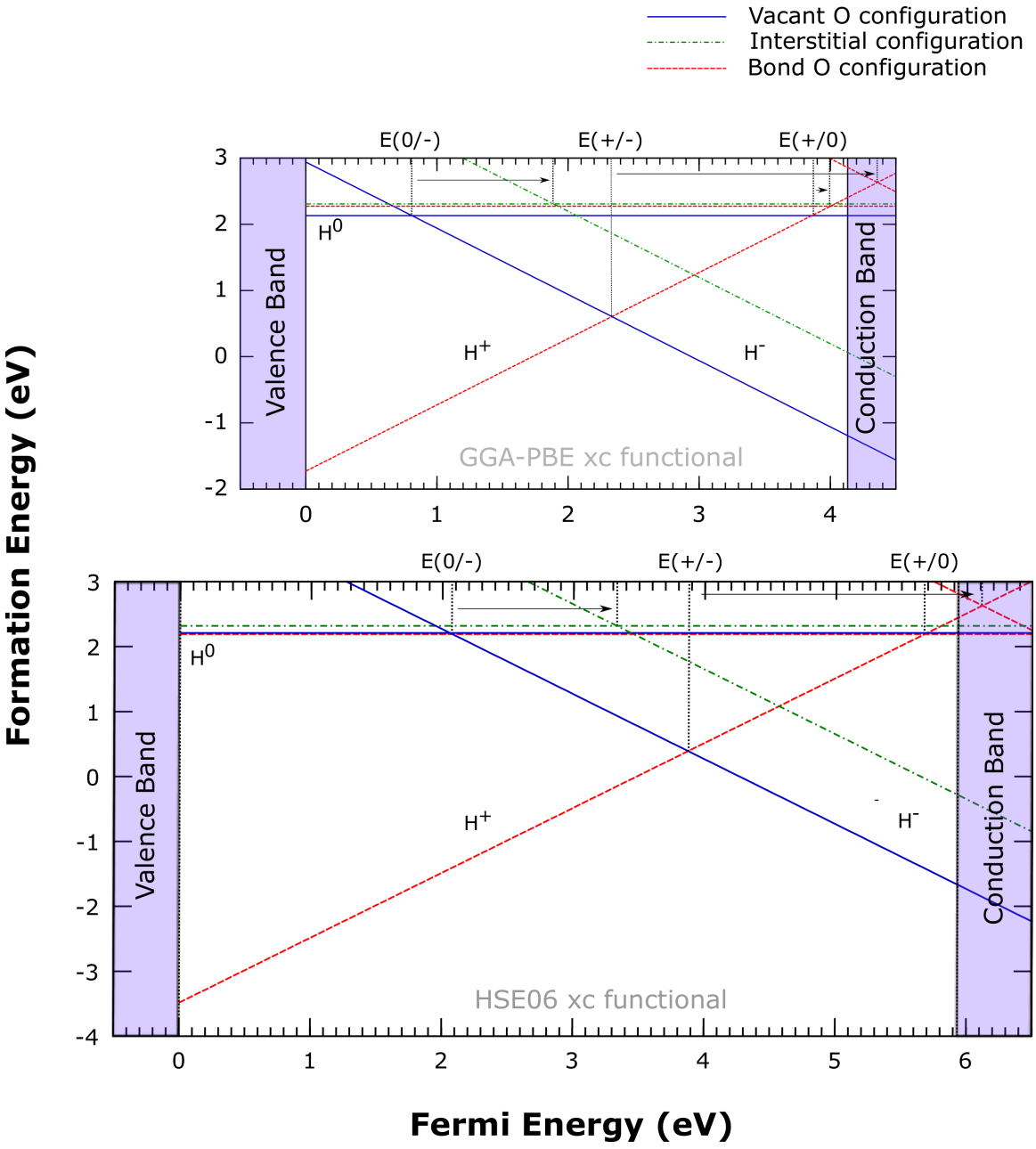

Figure 4.15: Formation energy of interstitial H as a function of the fermi level in Y_2O_3 for multiple geometrical configurations [4].

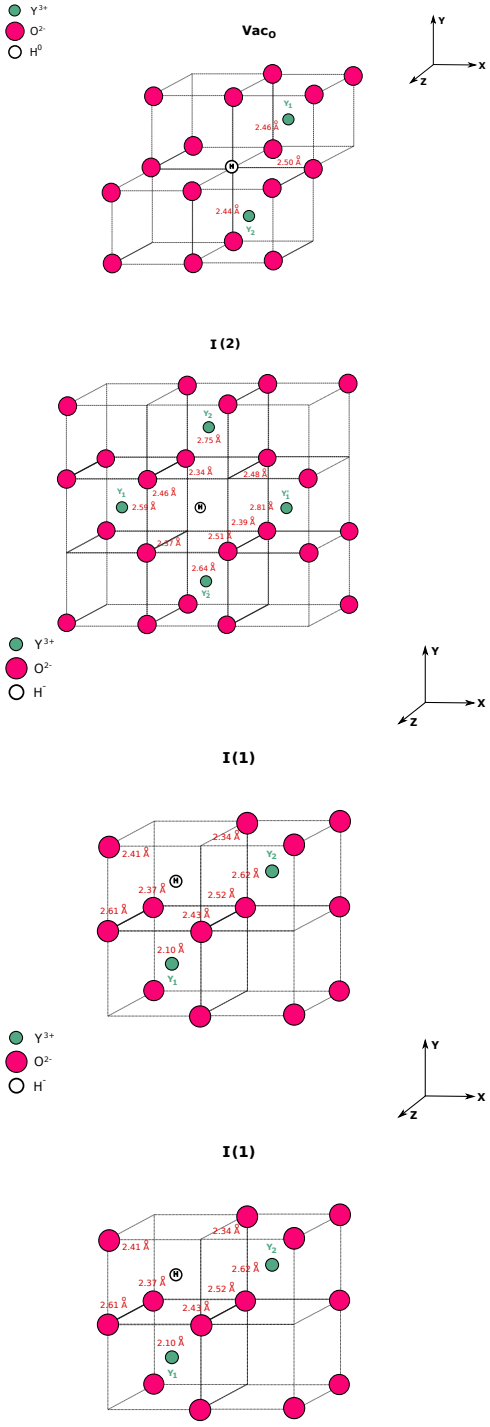

Figure 4.16: Representation of the H stable relaxed configurations for the three different charge states. The elements are represented by their ionic radius, where Y is represented by green, O is pink and H is white [4].

Bibliography

[1] S. F. J. Cox, J. L. Gavartin, J. S. Lord, S. P. Cottrell, J. M. Gil, H. V. Alberto, J. Piroto Duarte, R. C. Vilão, N. Ayres de Campos, D. J. Keeble, E. A. Davis, M. Charlton, and D. P. van der Werf. Oxide muonics: II. modelling the electrical activity of hydrogen in wide-gap and high-permittivity dielectrics. *Journal of Physics: Condensed Matter*, 18(3):1079, 2006.

[2] R. C. Vilão, A. G. Marinopoulos, R. B. L. Vieira, A. Weidinger, H. V. Alberto, J. Piroto Duarte, J. M. Gil, J. S. Lord, and S. F. J. Cox. Hydrogen impurity in paratellurite α-TeO_2: Muon-spin rotation and *ab initio* studies. *Phys. Rev. B*, 84(4):045201, Jul 2011.

[3] W. A. MacFarlane. βNMR and μSR as local magnetic probes of condensed mater. MPI-UBC, Stuttgat Quantum Materials "Summer" School, October 2010.

[4] E. L. Silva and A. G. Marinopoulos. Hydrogen impurity in yttria: *Ab-Initio* study by semi-local and hybrid functionals. *arXiv:1106.5032v1 [cond-mat.mtrl-sci]*, 2011.

[5] Fiolhais, Carlos; Nogueira, Fernando; Marques, Miguel A.L. A Primer in Density Functional Theory (Lecture Notes in Physics) (v. 620). Springer; 1 edition (2003).

[6] R C Vilão. *Isolated Hydrogen in II-VI Zinc-chalcogenide widegap semiconductors modelled by the muon analogue.* PhD thesis, Faculdade de Ciências e Tecnologia - Universidade de Coimbra, 2007.

[7] Stefan K. Estreicher. Hydrogen-related defects in crystalline semiconductors: a theorist's perspective. *Materials Science and Engineering: R: Reports*, 14(7-8):319 – 412, 1995.

[8] R.C. Vilão, J.M. Gil, A. Weidinger, H.V. Alberto, J. Piroto Duarte, N. Ayres de Campos, R.L. Lichti, K.H. Chow, and S.F.J. Cox. Information on hydrogen states in II-VI semiconductor compounds from a study of their muonium analogues. *Nuclear Instruments and Methods in Physics Research Section A: Accelerators, Spectrometers, Detectors and Associated Equipment*, 580(1):438 – 441, 2007. Proceedings of the 10 th International Symposium on Radiation Physics - ISRP 10.

[9] R. C. Vilão, J. M. Gil, A. Weidinger, H. V. Alberto, J. Piroto Duarte, N. Ayres de Campos, R. L. Lichti, K. H. Chow, S. P. Cottrell, and S. F. J. Cox. Acceptor level of interstitial muonium in ZnSe and ZnS. *Phys. Rev. B*, 77(23):235212, Jun 2008.

[10] A I Mansour, Z Salman, K H Chow, I Fan, P J C King, B Hitti, J Jung, and S P Cottrell. Dynamics and reactivity of positively charged muonium in heavily doped Si:B and comparisons with hydrogen. *Phys Rev Lett*, 100(25):257602, 2008.

[11] R E Pritchard, J H Tucker, R C Newman, and E C Lightowlers. Hydrogen molecules in boron-doped crystalline silicon. *Semiconductor Science and Technology*, 14(1):77, 1999.

[12] Vijay A. Singh, C. Weigel, J. W. Corbett, and L. M. Roth. Vibrational and electronic structure of hydrogen-related defects in silicon calculated by the extended huckel theory. *physica status solidi (b)*, 81(2):637–646, 1977.

[13] E. Cartier, J. H. Stathis, and D. A. Buchanan. Passivation and depassivation of silicon dangling bonds at the Si / SiO_2 interface by atomic hydrogen. *Applied Physics Letters*, 63(11):1510–1512, 1993.

[14] N.H. Nickel, editor. *Introduction to Hydrogen in Semiconductors II*, volume Semiconductor and Semimetals vol. 61. Academic Press, San Diego, 1999.

[15] B. Hitti, S. R. Kreitzman, T. L. Estle, E. S. Bates, M. R. Dawdy, T. L. Head, and R. L. Lichti. Dynamics of negative muonium in n-type silicon. *Phys. Rev. B*, 59(7):4918–4924, Feb 1999.

[16] S. F. J. Cox, E. A. Davis, S. P. Cottrell, P. J. C. King, J. S. Lord, J. M. Gil, H. V. Alberto, R. C. Vilão, J. Piroto Duarte, N. Ayres de Campos, A. Weidinger, R. L. Lichti, and S. J. C. Irvine. Experimental confirmation of the predicted shallow donor hydrogen state in zinc oxide. *Phys. Rev. Lett.*, 86(12):2601–2604, Mar 2001.

[17] S. R. Kreitzman, B. Hitti, R. L. Lichti, T. L. Estle, and K. H. Chow. Muon-spin-resonance study of muonium dynamics in Si and its relevance to hydrogen. *Phys. Rev. B*, 51(19):13117–13137, May 1995.

[18] B. Holm, K. Bonde Nielsen, and B. Bech Nielsen. Deep state of hydrogen in crystalline silicon: Evidence for metastability. *Phys. Rev. Lett.*, 66(18):2360–2363, May 1991.

[19] K. Bonde Nielsen, L. Dobaczewski, S. Søgård, and B. Bech Nielsen. Acceptor state of monoatomic hydrogen in silicon and the role of oxygen. *Phys. Rev. B*, 65(7):075205, Jan 2002.

[20] Conyers Herring, N. M. Johnson, and Chris G. Van de Walle. Energy levels of isolated interstitial hydrogen in silicon. *Phys. Rev. B*, 64(12):125209, Sep 2001.

[21] Chris G. Van de Walle, P. J. H. Denteneer, Y. Bar-Yam, and S. T. Pantelides. Theory of hydrogen diffusion and reactions in crystalline silicon. *Phys. Rev. B*, 39(15):10791–10808, May 1989.

[22] P. W. Anderson. Model for the electronic structure of amorphous semiconductors. *Phys. Rev. Lett.*, 34(15):953–955, Apr 1975.

[23] P. E. Blöchl. Projector augmented-wave method. *Phys. Rev. B*, 50:17953–17979, Dec 1994.

[24] Chris G. Van de Walle. Hydrogen as a cause of doping in zinc oxide. *Phys. Rev. Lett.*, 85(5):1012–1015, Jul 2000.

[25] J. M. Gil, H. V. Alberto, R. C. Vilão, J. Piroto Duarte, N. Ayres de Campos, A. Weidinger, J. Krauser, E. A. Davis, S. P. Cottrell, and S. F. J. Cox. Shallow donor muonium states in II-VI semiconductor compounds. *Phys. Rev. B*, 64(7):075205, Jul 2001.

[26] E. A. Davis, S. F. J. Cox, R. L. Lichti, and C. G. Van de Walle. Shallow donor state of hydrogen in indium nitride. *Applied Physics Letters*, 82(4):592–594, 2003.

[27] R. C. Vilão, H. V. Alberto, J. M. Gil, J. P. Piroto Duarte, N. Ayres de Campos, A. Weidinger, and M. V. Yakushev. Hydrogen states in $CuInSe_2$–a μSR study. *Physica B: Condensed Matter*, 340-342:965 – 968, 2003. Proceedings of the 22nd International Conference on Defects in Semiconductors.

[28] H. V. Alberto, A. Weidinger, R. C. Vilão, J. Piroto Duarte, J. M. Gil, J. S. Lord, and S. F. J. Cox. Mechanisms of electron polarization of shallow muonium in CdTe and CdS. *Phys. Rev. B*, 81(24):245205, Jun 2010.

[29] S. Suehara, P. Thomas, A. P. Mirgorodsky, T. Merle-Méjean, J. C. Champarnaud-Mesjard, T. Aizawa, S. Hishita, S. Todoroki, T. Konishi, and S. Inoue. Localized hyperpolarizability approach to the origin of nonlinear optical properties in TeO_2 -based materials. *Phys. Rev. B*, 70(20):205121, Nov 2004.

[30] E. Vorontsova, R. Grechishkin, I. Kaplunov, A. Kolesnikov, V. Molchanov, and S. Talyzin, I. et al. Manifestation of gyrotropy upon light scattering in paratellurite. *Optics and Spectroscopy*, 104:886–889, 2008. 10.1134/S0030400X08060143.

[31] V A Bagan, B L Davydov, and I E Samartsev. Characteristics of cornu depolarisers made from quartz and paratellurite optically active crystals. *Quantum Electronics*, 39(1):73, 2009.

[32] S. Beke, T. Kobayashi, K. Sugioka, K. Midorikawa, and J. Bonse. Time-of-flight mass spectroscopy of femtosecond and nanosecond laser ablated TeO_2 crystals. *International Journal of Mass Spectrometry*, 299(1):5 – 8, 2011.

[33] Zhifu Liu, Toshinai Yamazaki, Yanbai Shen, Toshio Kikuta, Noriyuki Nakatani, and Tokimasa Kawabata. Room temperature gas sensing of p-type TeO_2 nanowires. *Applied Physics Letters*, 90(17):173119, 2007.

[34] T. Siciliano, A. Tepore, G. Micocci, A. Genga, M. Siciliano, and E. Filippo. Transition from n- to p-type electrical conductivity induced by ethanol adsorption on α-tellurium dioxide nanowires. *Sensors and Actuators B: Chemical*, 138(1):207 – 213, 2009.

[35] C. Arnaboldi, C. Brofferio, A. Bryant, C. Bucci, L. Canonica, S. Capelli, M. Carrettoni, M. Clemenza, I. Dafinei, S. Di Domizio, F. Ferroni, E. Fiorini, Z. Ge, A. Giachero, L. Gironi, A. Giuliani, P. Gorla, E. Guardincerri, R. Kadel, K. Kazkaz, L. Kogler, Y. Kolomensky, J. Larsen, M. Laubenstein, Y. Li, C. Maiano, M. Martinez, R. Maruyama, S. Nisi, C. Nones, Eric B. Norman, A. Nucciotti, F. Orio, L. tavina, M. Pavan, G. Pessina, S. Pirro, E. Previtali, C. Rusconi, Nicholas D. Scielzo, M. Sisti, Alan R. Smith, W. Tian, M. Vignati, H. Wang, and Y. Zhu. Production of high purity TeO_2 single crystals for the study of neutrinoless double beta decay. *Journal of Crystal Growth*, 312(20):2999 – 3008, 2010.

[36] B. R. Sahu and Leonard Kleinman. Effect of atomic displacements on the ground state of α-TeO_2. *Phys. Rev. B*, 69(19):193101, May 2004.

[37] M. Ceriotti, F. Pietrucci, and M. Bernasconi. Ab initio study of the vibrational properties of crystalline TeO_2 : The α , β , and γ phases. *Phys. Rev. B*, 73(10):104304, Mar 2006.

[38] Yanlu Li, Weiliu Fan, Honggang Sun, Xiufeng Cheng, Pan Li, and Xian Zhao. Structural, electronic, and optical properties of alpha, beta, and gamma -TeO_2. *Journal of Applied Physics*, 107(9):093506, 2010.

[39] Yoshiro Ohmachi and Naoya Uchida. Temperature dependence of elastic, dielectric, and piezoelectric constants in TeO_2 single crystals. *Journal of Applied Physics*, 41(6):2307–2311, 1970.

[40] John Robertson. High dielectric constant gate oxides for metal oxide si transistors. *Reports on Progress in Physics*, 69(2):327, 2006.

[41] E. Hartmann and L. Kovács. Electrical conductivity of paratellurite (TeO_2) crystals. *physica status solidi (a)*, 74(1):59–64, 1982.

[42] A. Watterich et al. Electron spin resonance of Cr^{3+} and perturbed Cr^{3+} centers in α-TeO_2:Cr. *Journal of Physics and Chemistry of Solids*, 53(1):189 – 195, 1992.

[43] G J Edwards, O R Gilliam, R H Bartram, A Watterich, R Voszka, J R Niklas, S Greulich-Weber, and J M Spaeth. An electron spin resonance study of vanadium-doped α-TeO_2 single crystals. *Journal of Physics: Condensed Matter*, 7(15):3013, 1995.

[44] S. G. Karshenboim. Constraints on a long-range spin-dependent interaction from precision atomic physics. *Phys. Rev. D*, 82(11):113013, Dec 2010.

[45] Randolf Pohl, Aldo Antognini, François Nez, Fernando D. Amaro, François Biraben, João M. R. Cardoso, Daniel S. Covita, Andreas Dax, Satish Dhawan, Luis M. P. Fernandes, Adolf Giesen, Thomas Graf, Theodor W. Hänsch, Paul Indelicato, Lucile Julien, Cheng-Yang Kao, Paul Knowles, Eric-Olivier Le Bigot, Yi-Wei Liu, José A. M. Lopes, Livia Ludhova, Cristina M. B. Monteiro, Françoise Mulhauser, Tobias Nebel, Paul Rabinowitz, Joaquim M. F. dos Santos, Lukas A. Schaller, Karsten Schuhmann, Catherine Schwob, David Taqqu, João F. C. A. Veloso, and Franz Kottmann. The size of the proton. *Nature*, 466(7303):213–216, July 2010.

[46] David Tucker-Smith and Itay Yavin. Muonic hydrogen and MeV forces. *Phys. Rev. D*, 83(10):101702, May 2011.

[47] J. M. Bailey, W. E. Cleland, V. W. Hughes, R. Prepost, and K. Ziock. Muonium. II. observation of the muonium hyperfine-structure interval. *Phys. Rev. A*, 3(3):871–884, Mar 1971.

[48] W. Liu, M. G. Boshier, S. Dhawan, O. van Dyck, P. Egan, X. Fei, M. Grosse Perdekamp, V. W. Hughes, M. Janousch, K. Jungmann, D. Kawall, F. G. Mariam, C. Pillai, R. Prigl, G. zu Putlitz, I. Reinhard, W. Schwarz, P. A. Thompson, and K. A. Woodle. High precision measurements of the ground state hyperfine structure interval of muonium and of the muon magnetic moment. *Phys. Rev. Lett.*, 82(4):711–714, Jan 1999.

[49] C. J. Joachain B. H. Bransden. *Physics of Atoms and Molecules*. Prentice Hall, Harlow, 2nd edition edition, 2003.

[50] Bruce D. Patterson. Muonium states in semiconductors. *Rev. Mod. Phys.*, 60(1):69, Jan 1988.

[51] G. Breit and I. I. Rabi. Measurement of nuclear spin. *Phys. Rev.*, 38(11):2082–2083, Dec 1931.

[52] R. H. Landau. *Quantum Mechanics II*. John Wiley & Sons, Inc., New York, 1996.

[53] A Schenck. *Muon Spin Rotation Spectroscopy: Principles and Applications in Solid State Physics*. Adam Hilger Ltd, Bristol, 1985.

[54] M. C. Lynch, S. P Cottrell, P. J. C King, and G. H. Eaton. Measuring small samples at the isis muon source. *Physica B: Condensed Matter*, 326(1-4):270 – 274, 2003.

[55] R. Abela, A. Amato, C. Baines, X. Donath, R. Erne, D.C. George, D. Herlach, G. Irminger, I.D. Reid, D. Renker, G. Solt, D. Suhi, M. Werner, and U. Zimmermann. Muons on request (more): combining

advantages of continuous and pulsed muon beams. *Hyperfine Interactions*, 120-121:575–578, 1999. 10.1023/A:1017046817431.

[56] H. Jain and A. S. Nowick. Electrical conduction in paratellurite (TeO_2) crystals. *physica status solidi (a)*, 67(2):701–707, 1981.

[57] F. L. Pratt. Wimda: a muon data analysis program for the windows pc. *Physica B: Condensed Matter*, 289-290:710 – 714, 2000.

[58] J. M. Gil, P. J. Mendes, L. P. Ferreira, H. V. Alberto, R. C. Vilão, N. Ayres de Campos, A. Weidinger, Y. Tomm, Ch. Niedermayer, M. V. Yakushev, R. D. Tomlinson, S. P. Cottrell, and S. F. J. Cox. Modeling hydrogen in $CuInSe_2$ and $CuInS_2$ solar cell materials using implanted muons. *Phys. Rev. B*, 59(3):1912–1916, Jan 1999.

[59] S F J Cox. Muonium as a model for interstitial hydrogen in the semiconducting and semimetallic elements. *Reports on Progress in Physics*, 72(11):116501, 2009.

[60] R.C. Vilão, J.M. Gil, A. Weidinger, H.V. Alberto, J. Piroto Duarte, B.F.O. Costa, N. Ayres de Campos, R.L. Lichti, K.H. Chow, S.P. Cottrell, and S.F.J. Cox. Delayed electron capture and μ^- formation in ZnSe. *Physica B: Condensed Matter*, 404(5-7):888 – 891, 2009. Proceedings of the Eleventh International Conference on Muon Spin Rotation, Relaxation and Resonance.

[61] R.L. Lichti, B.R. Carroll, J.E. Vernon, H.N. Bani-Salameh, K.H. Chow, I. Fan, M. Egilmez, R.C. Vilão, J.M. Gil, H.V. Alberto, J. Piroto Duarte, N. Ayres de Campos, S.P. Cottrell, and S.F.J. Cox. Possible donor and acceptor energies for mu in ZnSe. *Physica B: Condensed Matter*, 404(5-7):827 – 830, 2009. Proceedings of the Eleventh International Conference on Muon Spin Rotation, Relaxation and Resonance.

[62] J.S. Lord. Computer simulation of muon spin evolution. *Physica B: Condensed Matter*, 374-375:472 – 474, 2006. Proceedings of the Tenth International Conference on Muon Spin Rotation, Relaxation and Resonance.

[63] I. G. Ivanter and V. P. Smilga. The theory of μ^+ - meso depolarization with allowance for process of charge exchange or formation of unstable species. *Soviet Physics JETP*, 33(1030), 1971.

[64] V. G. Nosov and I. V. Yakovleva. Depolarization of μ^+ mesons in solids. *Soviet Physics JETP*, 16(1236), 1963.

[65] J. Piroto Duarte. *Study of hydrogen in phthalocyanine semiconductors using μSR techniques*. PhD thesis, Universidade de Coimbra, 2006.